Manipulation of the Motion of Polyatomic Molecules in the Rotational Ground State

Microwave Lens Effect by AC Stark Dipole Force

by

Wei Zhong

B.Sc., Wuhan University, 2011

A THESIS SUBMITTED IN PARTIAL FULFILLMENT OF
THE REQUIREMENTS FOR THE DEGREE OF

MASTER OF SCIENCE

in

The Faculty of Graduate and Postdoctoral Studies

(Physics)

THE UNIVERSITY OF BRITISH COLUMBIA

(Vancouver)

October 2013

Abstract

The main contribution of this project to the field of cold and ultracold molecules is we firstly demonstrated successful manipulation of the motion of polyatomic molecular beam in the rotational ground state, which has the lowest temperature of all possible states. Chapter 1 gives a summary of this field, including the application of cold and ultracold molecules, the methods to obtain them, and each method's advantages and disadvantages. Once we decelerate molecular ensembles, we would like to trap the cold and ultracold molecules in electric trap, megnetic trap and megneto-optical trap. Chapter 2 starts with an introduction of the concept of supersonic beam and the basic knowledge of it, such as the specific features. The experimental setup will also be presented and explained in this chapter. The main highlight of this project is that we are manipulating molecules in the real ground state. Our molecular source is a Counter Rotating Nozzle(CRN), which can precool (or slow in alternate terminology) molecules in all states including the rotational ground state. The principle and performance of CRN will be presented and explained in Chapter 3. After obtaining a well precooled molecular beam, the microwave lens effect on various species is presented in Chapter 4. Meanwhile, the principle of AC Stark shift, AC dipole force and the microwave standing wave modes, such as TE modes and TM modes, will be explained in this chapter as well. Finally, I'll summarize, draw conclusion of this work and describe the future expectation of this project in Chapter 5.

Preface

Statement of relative contributions

The construction of the experimental setup including the source chamber (Counter Rotating Nozzle), microwave chamber and detection chamber was done by Pavle Djuricanin. Some advice on the design of CRN came from Professor Frank Stienkemeier's group and improvement was done by Pavle Djuricanin. The microwave cylindrical tube was mainly designed by Pavle Djuricanin, Katsunari Enomoto, Omid Nourbakhsh and Ilja Gerhardt. The detection chamber was designed by Pavle Djuricanin. The cooling system, liquid nitrogen tank was designed by Mr. Djuricanin, and was made by Jorgen Hansen and Pritesh Padhiar at the Technical Services at UBC. The ion optics chamber was designed and assembled by Steffen Spieler. I did theinitial analysis of molecular source beam features from CRN. The experimental parameters were optimized by Steffen Spieler, Pavle Djuricanin and I. I was responsible for conducting the experiments, improving the experiments, collecting and analyzing the data. The CH3CN lens effect simulation with TM mode was done by Steffen Spieler. A notch filter was designed and made by Steffen Spieler. I made and tested the shutter which improved the system vacuum. I carried on the simulation of CD3CN lens effect with TE mode based on previous work. The resulting publication[1] was written by Professor Takamasa Momose.

Publication arising from thesis work

This thesis work has produced the following publication:

S. Spieler, W. Zhong, P. Djuricanin, O. Nourbakhsh, I. Gerhardt, K.Enomoto, F. Stienkemeier and T. Momose. Microwave lens effect for the J = 0 rotational state of CH_3CN. Molecular Physics, 111:1823-1834, 2013

Table of Contents

List of Figures

Acknowledgements

Before I came to UBC and this laboratory, I have to say I was not well prepared, neither for overseas life as an international student, nor research background knowledge. Even though I encountered dozens of problems at the beginning, assistance from friends, colleagues and supervisor help me out. As a result, this thesis has come out finally. First and foremost, I'd like to thank Professor Momose for offering me an opportunity to conduct research in his group and finish my Master's degree in physics here. I appreciate his patience, trust and valuable advice to guide me on the research. I appreciate he assisted me financially to attend the Gordon Rearch Conference in 2012 and Canadian Association of Physists Congress in 2013, where I broadened my view on physics science and acquired lots of new knowledge. These experiences are invaluable for a master student like me.

Mr. Djuricanin is the technician of our lab, and probably the best technician I have met or will meet in my whole life. With full-picture and comprehensive knowledge of projects in our lab, he could always stand out whenever problems rise. His solid backup, hard working and constructive disscusion has accelerated the progress of this whole project.

Our postdoc, Dr. Yang Liu, offered accurate theoretical assistance, to make me understand the experimental results. Our discussion at lunch time inspired me a lot to come up with solutions and improvments. I would like to thank Eric's help with my thesis and understanding of the native culture.

Also, I appreciate the former work from Omid Nourbakhsh, Ilja Gerhardt and Katsunari Enomoto, without whose work, I couldn't have received this well-prepared experimental setup.

Finally, I appreciate the support from Technical Services at UBC.

Dedication

I appreciate my friends' suggestion and spiritual encouragement in the past two years. The time we spent together made the life here so enjoyable, and inspired me to think about the research and be active in preparing this thesis.

I would like to thank my family, Shihui Zhong, Xian Zhong, You Zhong, Huazhen Wang and Jikuan Zhong, for their support on my education financially and spiritually.

Chapter 1

Introduction

Last year, the Nobel Prize in physics was awarded to Dr. Serge Haroche and Dr. David J. Wineland for "ground-breaking experimental methods that enable measuring and manipulation of individual quantum systems". Dr. David J. Wineland traps electrically charged atoms, or ions, controlling and measuring them with light, or photons. In the opposite approach, Dr. Serge Haroche controls and measures trapped photons, or particles of light, by sending atoms through a trap[2]. Nowadays, lots of researchers around all over the world are working on cold($1mK$-$1K$) and ultracold($<1mK$) molecules, decelerating the molecular beam, trapping it, and conducting research on it. Then, why are cold and ultracold molecules so hot now? The research field of cold molecules brings together two of three main thrusts of modern atomic, molecular and optical (AMO) physics: the ultracold and the ultraprecise. It also brings together researchers from a variety of fields, including AMO physics, chemistry, quantum information science and quantum simulations, condensed matter physics, nuclear physics and astrophysics[3]. It is widely recognized that cold and ultracold molecules play an important role in basic scientific exploration[4–10]. Their application includes the realization of Bose-Einstein condensation [11], study of molecular collision and cross sections at ultralow temperatures[12, 13], knowledge of ultracold chemical rates[14, 15], measurement of the electron's electric dipole moment[16], superchemistry[17], and quantum computation[18]. Considering the significance of cold and ultracold molecules, researchers have developed several methods to obtain them; each of them has its own advantages and disadvantages. Laser cooling of atoms technique is well developed, but not well extended to molecules because of their complex internal stucture. For laser cooling, an almost closed transition is required, which can be found in many atoms, but is very demanding in the case of molecules[19]. Recently, success of laser cooling of a diatomic molecule was reported and it has bridged the gap between ultracold(submillikelvin) temperature and the $1K$ temperature attainable with directly cooled molecules[20]. Another way to obtain ultracold molecules is to laser cool atoms to ultracold regime and photoassociate them into ultracold molecules[21, 22]. The direct cooling

methods includes Stark decelerator[23–25], Zeeman decelerator[26], sympathetic cooling[27, 28], Sisyphus cooling[29], buffer gas cooling[30, 31], and the methods we'll discuss later, the CRN[32–38], and mcrowave decelerator[39–45]. In order to enhance the phase space density, guide technologies are applied on the decelerated molecular beam[46, 47]. After deceleration, various traps[48–53] are need to hold the ensemble for further research as mentioned above.

In this thesis, CH_3CN and CD_3CN in ground states are the target molecules and their energy levels are explored. The sample is seeded in krypton carrier gas with pressure of $3bar$. The supersonic molecular beam is created after the open valve. First, we slow down the internal-cooled supersonic beam's translational velocity from $400m/s$ to about $100m/s$ by CRN. Then, when flying through the microwave resonator, a cylindrical cavity, the motion of molecular beam is manipulated by the AC Stark dipole force produced by standing wave, either focusing or deceleration. The focusing is realized with standing wave in both of TM_{01p} and TE_{11p} modes, and deceleration could be realized with that in TE_{11p} mode because of its three-dimensional potential trap[42]. A superconducting cylindrical tube is needed in the future for deceleration since the requirement of high quality factor. The achieved maximum electric field in the tube is about E0/2=$11kV/cm$. Two different detection techniques are used. One of them is RGA (Residual Gas Analysis) detection, and the other one is MCP (Microchannel Plate) detection. Also, the trajectory and time-of-flight simulation results by a fourth order Runge-Kutta algorithm support experimental data very well.

Chapter 2

Supersonic beam and experimental setup

The object we are studying is the molecular beam essentially. Therefore, we'll briefly introduce supersonic molecular beam and the questions which need to be answered in this chapter: for exmaple, how to create supersonic beam, what's the feature of it, and the reason why supersonic molecular beam is choosen, in order to show a basic picture of supersonic molecular beams. After that, the whole experimental setup will be presented, as well as the function of each part, including the source chamber(CRN), the microwave chamber, the detection chamber, the microwave generator, the vacuum system, the control system and so on.

2.1 Supersonic molecular beam

The cooling methods we mentioned in Chapter 1 are mainly about how to cool the translational degrees of freedom. However, before that, the very first step is to make an internally cooled molecular beam source. During the expansion of a gas through a supersonic nozzle, rotational cooling occurs through equilibration with the geometrically cooled translational degrees of freedom via collisional energy transfer[54]. The following diagram, Figure 2.1[55], shows the features of supersonic beam in space dimension.

A free-jet molecular beam can be produced by supersonic expansion from high pressure to low pressure, provided the ratio of p_0/p_b exceeds the critical value[55], where p_0 is pressure in the gas line and p_b is that of background.

$$G = (\frac{\gamma+1}{2})^{\frac{\gamma}{\gamma-1}} \tag{2.1}$$

γ is defined as γ=c_p/c_v, where c_p is molar heat capacity of ideal gas at constant pressure and c_v is that at constant volume. A supersonic beam has several important characteristic properties. First, the beam velocity, in

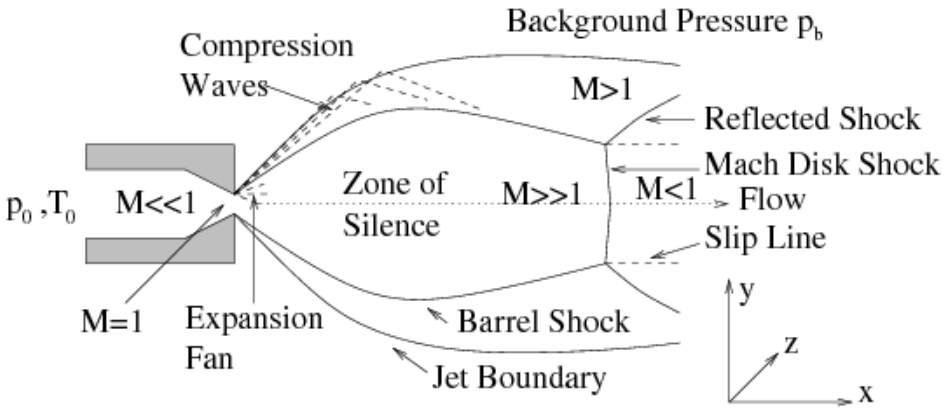

Figure 2.1: There are separate zones distinguished by velocities of the molecular beam. The Zone of Silence is the desired one in our experiments.

dimensionless unit of M, increases during the expansion. Second, the beam parameters in the zone of silence are independent of boundary conditions[55], which means the velocity of molecules in the zone of silence will be much larger than the speed of sound regardless of background pressure p_b.Third, the longitudinal velocity distribution width of the beam is very narrow. Fourth, the beam maintains a good directionality, with small transverse velocity.

2.2 Experimental setup

In this thesis, our first goal was the manipulation of motion of polyatomic molecules in rotational ground state. How does it actually be achieved? In figure 2.2, a cartoon of lens effect on the molecular beam is shown. The molecular beam comes out from the nozzle moving backward with velocity of $300m/s$. The slowed molecular beam colored in green is focused by the AC stark dipole force. The red and blue disks reprensent the standing wave nodes where the maximum of field strength is obtained.

Experimental setup is illustrated in Figure 2.3, which consists of three sections: A CRN, a microwave cavity, and a detector. A titanium nozzle with an orifice of $200\mu m$ was attached to one end of a carbon-fiber tube with an inner diameter of $2.5mm$ and a outer diameter of $4.0mm$, and rotated by a brushless DC-Servomotor (Faulhaber, 2057S012BK179) in a vacuum chamber. The center of the rotor was attached to a ferrofluidic feedthrough for the introduction of gases inside the tube. The arm of the carbon-tube that did not have the titanium nozzle was plugged with a carbon-fiber rod in order to prevent any gas flow into this side of the arm, while keeping the balance of the rotor. The frequency of the spindle rotation was monitored by a diode laser. The rotor tip speed was continuously variable between $10m/s$ and $320m/s$.

One advantage of our source chamber is that we have installed a pulsed valve instead of utilizing a continuous gas inlet in order to reduce the background pressure during operation, so that the pumping requirement is reduced dramatically. A pulsed valve (General Valve, 9 Series) was attached at the inlet of the ferrofluidic feedthrough to allow for a pulsed rotating source so that the gas load to the turbo pump is minimized. The valve was operated with an opening time of $450\mu s$ at repetition time of $5s$ and backing pressure of $3bar$.

Our source chamber is pumped by a $800l/s$ turbo pump and detection chamber is pumped by a $300l/s$ turbo pump.The background pressure in

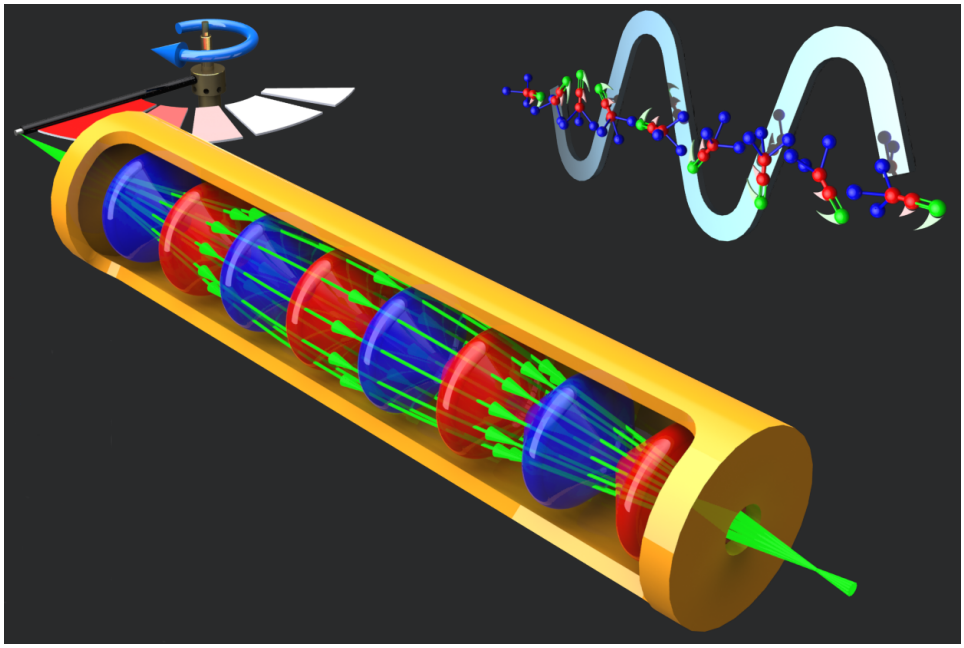

Figure 2.2: The microwave field is polarized and motion trajectories of polyatomic molecules are deflected due to the AC dipole force, the so-called lens effect

source chamber can maintain as low as 10^{-7} *torr* between successive pulsing. The range of pressure change is from 10^{-7} to 10^{-4} *torr* when pulsing.

The source chamber and the microwave cavity were sperated by a skimmer (Beam Dynamics, $3mm$ orifice). A home-made shutter was installed before the skimmer to pick up only the first pulse after the introduction of the gas into the tube and block the rest of the beam in order to reduce the gas load.

The microwave cavity is made of copper. The cavity was constructed from a $400mm$ long, $12.6mm$ inside diameter copper tube and two copper end caps with a thickness of $4mm$, Each end cap had a hole at the center to let molecular beam pass. The diameter of entrance hole is $6mm$ and that of exit hole is $4.5mm$. A teflon disk with a thickness of $3mm$ was additionally placed at the center of the cavity to separate the cavity into two sections. The teflon disk had a hole of $5mm$ in diameter at the center in order to enhance the signal of the $J = 0$ ground state.

There are another two holes in the side of the copper tube for the placement of coupling loop antennas made from semi-rigid coaxial cable (Coax, SC-219/50-SCN-CN). One of them transmitted high power into the microwave cavity while the other monitored the resonant frequency. The depth of insertion of both antennas is adjustable to find the best coupling condition and high $Q\text{-}factor$. The loss of the MW power due to the coaxial cable was estimated to be about 50%∼60%. The cavity was cooled by a liquid nitrogen tank to reduce the surface resistance and thereby to increase the $Q\text{-}factor$ of the cavity as high as $1{\sim}1.5{\times}10^4$ for each mode.

The microwave signal was generated by a synthesizer (Anritsu MG3693C), and amplified by a traveling wave tube amplifier (Hughes 1277H04F000). The maximum output power of the amplifier is $10W$.

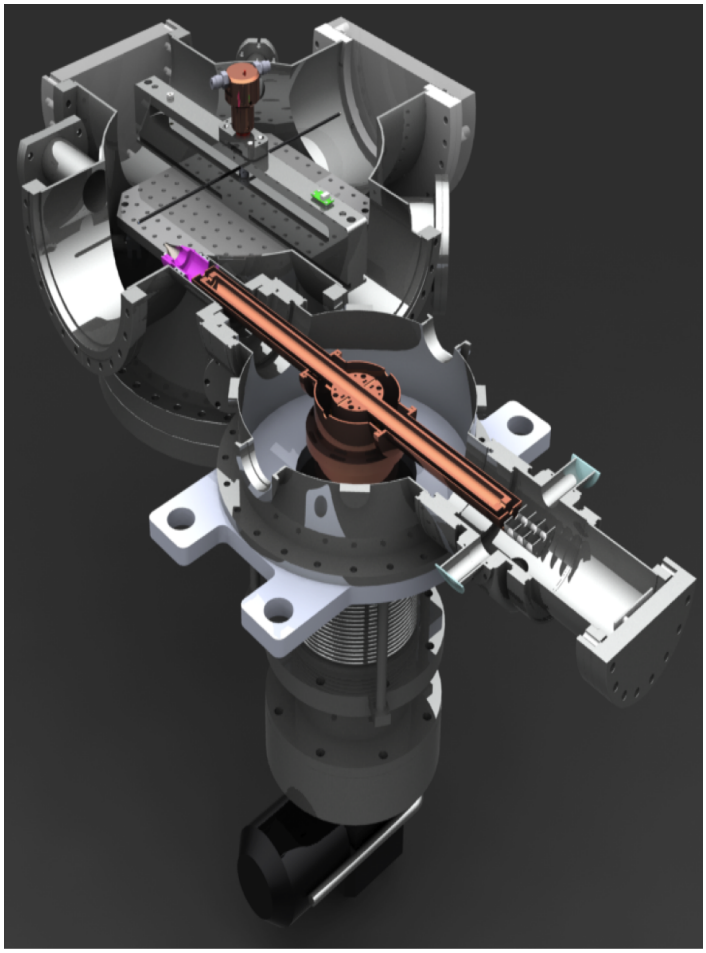

Figure 2.3: The experiment system consists of three chambers, the CRN source chamber, the microwave chamber and the detection chamber.

2.2.1 The shutter

In order to improve the vacuum in MW chamber and detection chamber, a shutter has been installed. The skimmer can prevent molecules off the axis from going into the next chamber. The problem is, when valve is open, each rotation of nozzle will generate a beam pulse going into the MW cavity. However, we found the first pulse had the best characheristic properties of a supersonic molecular beam, stronger intensity and narrow velocity spread. The home-made shutter completed this mission essentially. It's made of a hard drive magnetic switch as shown in figure 2.4. Once the first pulse came through the skimmer, the shutter was closed in front of the skimmer, blocking the following beam pulses and keeping them in the source chamber where a stronger turbo pump was located. According to the testing, the shutter can close the entrance completely in about $10ms$. By varying the delay time compared to the synchronization or pulsing timing, it can allow the first pulse to go through and block the second one perfectly. With this work, the background pressure remained at 10^{-8} *torr* in detection chamber even when pulsing.

2.2.2 The rotor and nozzle

In our experiment, the rotor will be sped up to about $300m/s$, close to the speed of sound, so a rotor made of carbon fiber was chosen for its high strength. The length from the tip to the spindle is about $19cm$. It was glued onto the shaft and a titanium ferrule was attached to the long end, while opposite end had carbon fiber rod inserted and glued. The position of rod is adjusted for careful static balancing of rotor. Titanium ferrule incorporated a step such that the nozzle output diameter might be changed by gluing an aperture over the $250um$ hole as shown in figure 2.6. The step also helped align the nozzle perpendicular to the spindle. The length of the carbon fiber tube is about $36cm$.

A large brass block sits on an aluminum housing piece to dampen vibration. Figure 2.7 shows the vibration noise when increasing the rotation speed. There is a minima appearing around $260Hz$ which we have focused on. The valve and ferrofluidic feedthrough are coupled through aluminum ferrule that fits closely into housing. The spindle (titanium) O-ring is sealed to ferrofluidic shaft. The opposite side of spindle is coupled to motor with soft silicone tubing. A large copper block attached to the motor is water-cooled to remove excess heat from motor.

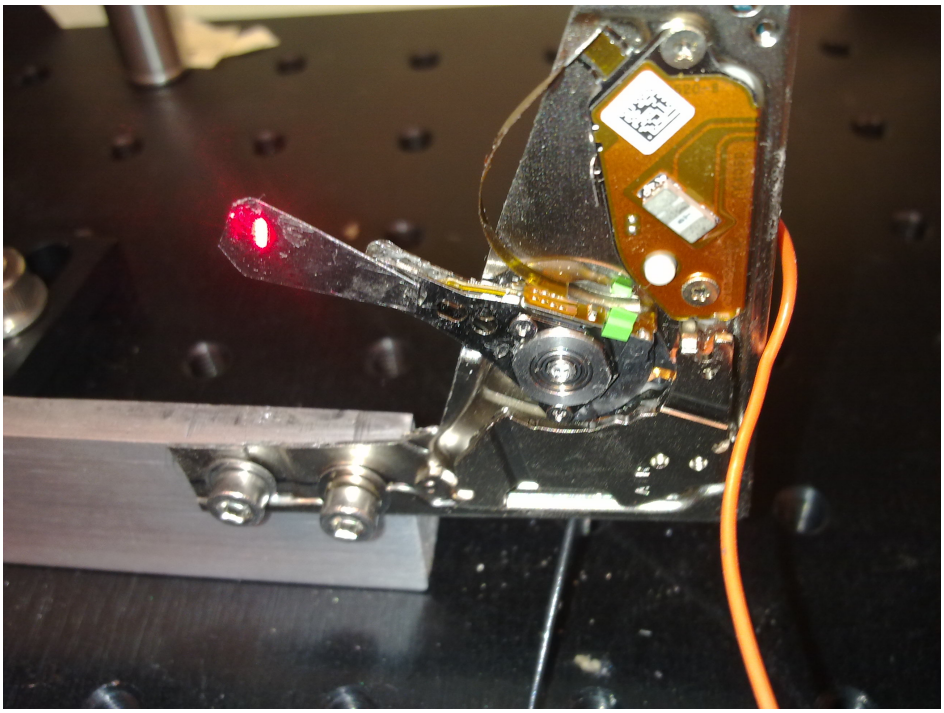

Figure 2.4: The shutter under testing

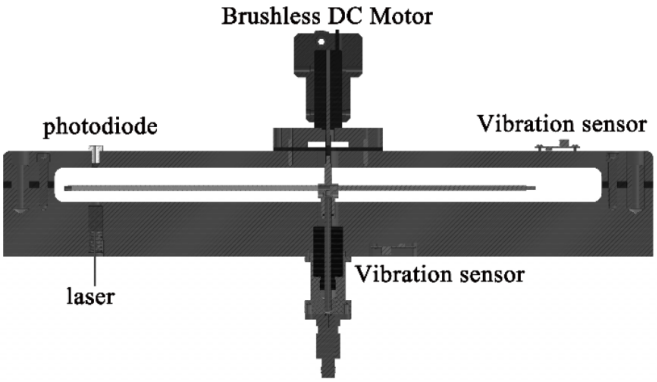

Figure 2.5: The rotor

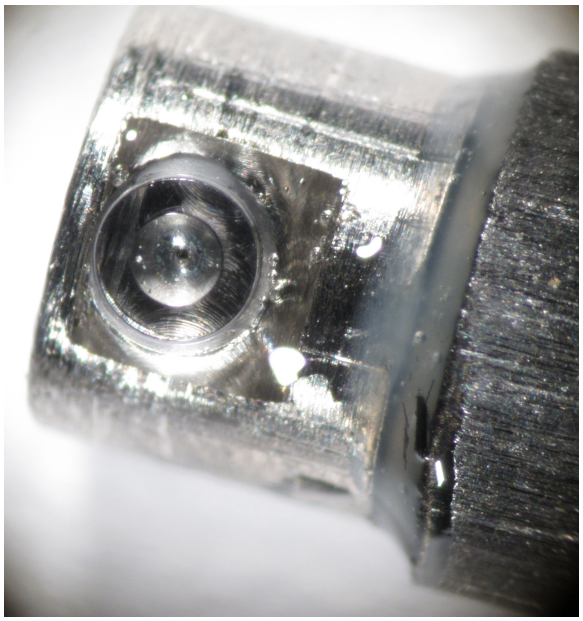

Figure 2.6: The nozzle

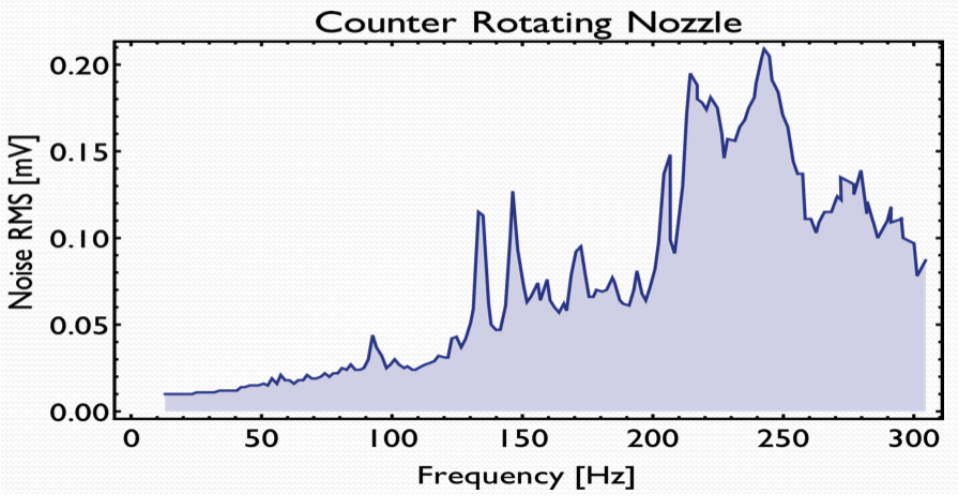

Figure 2.7: The vibration with different frequencies

2.2.3 The microwave tube

The core part of the microwave cavity is the cylindrical cavity tube of copper as shown in figure 2.8. The length of this cavity is about $408mm$ at room temperature and the radius is about $7mm$.

Figure 2.8: The copper cylindrical cavity

A strong electrical field with amplitude of up to about $600kV/m$ is applied in the tube with input power of $20W$. In order to obtain such strong field, a liquid nitrogen cooling system is attached to the tube to decrease the surface resistance. When temperature is down to $77K$, the tube is about $6.3mm$ in radius and $400mm$ in length. The quality factor of a cavity is defined generally as $Q = 2\pi vW/P$, where v is the microwave frequency, W is the total energy stored in the cavity and P is the power loss of the cavity. The $Q\text{-}factor$ is up to about 10^4. We focused on TM_{01p} and TE_{11p} modes and figure 2.9 shows the spectrum of TE_{11p} modes for our microwave cavity. Since a travelling-wave tube (TWT) amplifier was utilized to increase input power, the possible frequency shift after the amplifier was considered. It

showed the frequency shift is not observable up to order of $1MHz$, so the effects could be ignored in this situation.

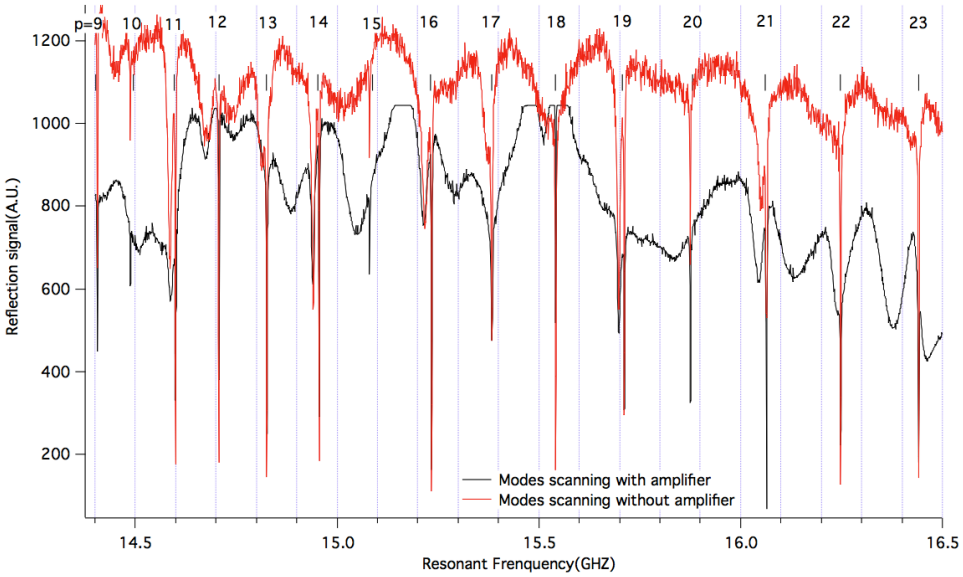

Figure 2.9: The TE_{11p} mode spectrum

The mode was assigned by fitting the length and radius to equation 2.2, and the nodes number p was aquired.

$$v = \frac{c}{2}\sqrt{(\frac{x_{lm}}{a\pi})^2 + (\frac{p}{L})^2} \tag{2.2}$$

where c is the light speed, $x_{lm}$is 2.4048 for TM_{01p} modes and 1.8412 for TE_{11p} modes, p is the node number of standing wave, a is the radius and L is the length of the microwave tube. When calculating the nodes, we must take the contraction of the cavity caused by the low temprature($77K$) into consideration. Take the length for example: it contracted by $8mm$ from $408mm$ to $400mm$. This layout change is considered in the simulation section as well.

2.2.4 The detection

Two different detection techniques are utlized in our experiment. The first one is MCP detection and the other one is RGA detection

The MCP detector

When molecular beam arrives at the laser focal point, the molecules will be ionized and charged. An electric field for accelerating charged particles is built using ion optics. The arriving timing of particles with different charge-to-mass ratios are different. Each time when the charged particle hits the wall of the microchannel of MCP detector, more electrons will be ejected like an avalanche so that a weak signal will be detectable.

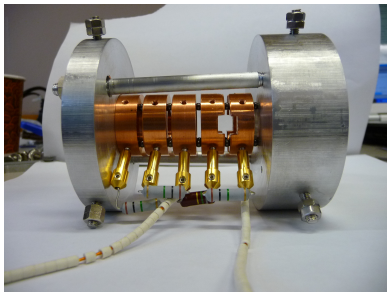

Figure 2.10: The ion optics

Figure 2.11: The MCP detector

The RGA dector

RGA[1] is a mass spectrometer with small physical dimensions that can be connected directly to a vacuum system and whose function is to analyze the gases inside the vacuum chamber. It can distinguish charged particles according to the different charge-to-mass ratio.

It consists of three modules. First is an ion source, which can convert gas phase sample molecules into ions. Second is a mass analyzer(filter), which sorts the ions by their charge-to-mass ratio by applying electromagnetic fields. The last is a detector, which measures the value of an indicator quantity and thus provides data for calculating the abundances of each ion present. Here is the way how it works: when a sample is loaded into the RGA and undergoes vaporization, the components of the sample are ionized, and the ions are separated according to their mass-to-charge ratio in an analyzer by electromagnetic fields. Finally the ions are detected, usually by a quantitative method, and then processed into mass spectra.

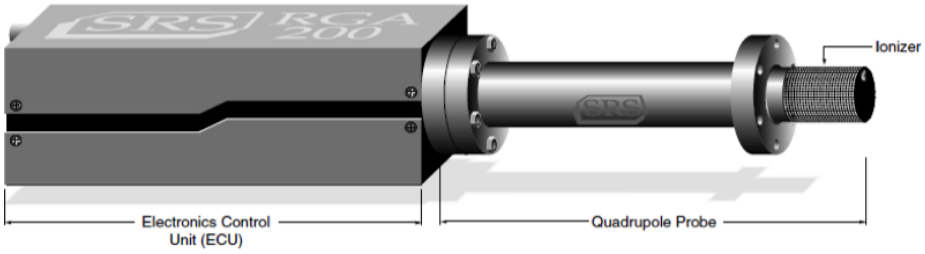

Figure 2.12: The RGA

The ionization section of the RGA was placed about $6cm$ behind the exit hole of the microwave cavity. The advantage of the RGA is that it has a large detection area which can enhance the detected signal. It is even a better choice when considering the non-trivial alignment of the molecular beam produced by CRN.

A trasimpedance amplifier followed by a voltage amplifier (Standford Research, SR570 and SR560) was connected to the RGA. The amplified signal was record in real time by an oscilloscope (Agilent DSO5034A). A home-made notch filter was used to reduce the noise.

[1] We used a Model SRS100 RGA

Chapter 3

Molecular beam source: Counter Rotating Nozzle

The highlight of this work is the beam source we use, CRN. In order to manipulate the molecular beam, we need to precool and slow the beam down to about $100m/s$. The Stark decelerator was used in Gerard Meijer's group[44]. According to Earnshaw's theorem, there are no local minima or maxima of the field potential in free space by static field. Therefore, the target molecular states are limited to the low field seeking state (LFS), which is not the rotational ground state. Our advantage is that CRN can slow target gas-phase molecules in all states regardless of the molecular mass.

3.1 The principle of CRN in slowing molecular beams

The CRN is a mechanical method to produce intense cold, slow beams of atoms and molecules, which utilizes the peripheral backward velocity of a high-speed rotating nozzle to offset the beam's velocity. By changing the rotating speed of the nozzle, velocity of the beam can be easily tuned.

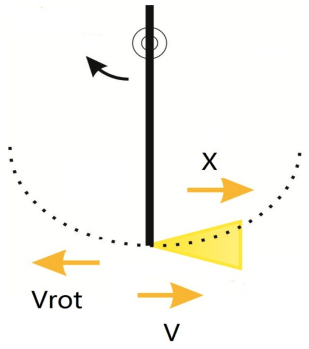

Figure 3.1: The Principle of CRN

As the nozzle moves backward relative to the molecular beam motion, the beam velocity is reduced to V=X-V_{rot}, where X is the initial velocity of the molecular beam and V_{rot} is the velocity of nozzle. The difficulty for existing systems which use a continuous gas inlet is the requirement of a large pumping capacity[35, 38]. To overcome this issue, a pulsed valve was installed at the spindle in order to reduce the background pressure during operation as mentioned above.

3.2 Properties of molecular beams created by CRN

Figure 3.2 shows the original signal of the Argon pulse train with a rotation rate of $100Hz$. When the valve was open, one beam pulse was produced per rotation. As the time went by, the pressure in the nozzle became lower so that the intensity of pulses decreased. The background pressure increased at the beginning, then decreased as the gas was pumped out.

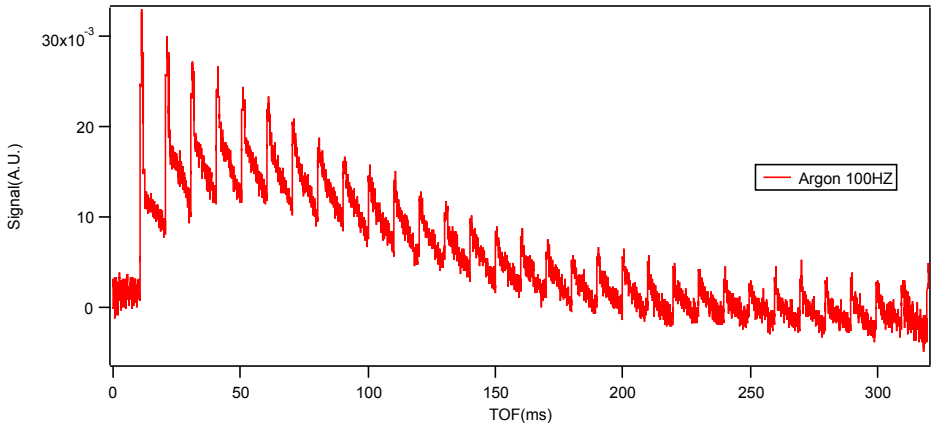

Figure 3.2: The pulse train

The first pulse, with the strongest intensity and the lowest background pressure, is enlarged and depicted in figure 3.3. We noticed a high frequency oscillation which showed up in the baseline. This noise source was due to the vibration of the turbo pumps and the rotor.

After the first pulse, the intensity of following pulses decreased exponentially as illustrated in figure 3.4

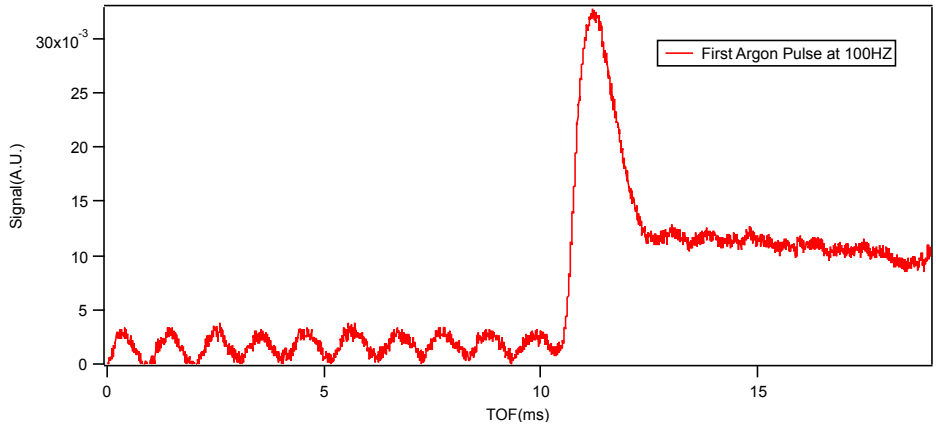

Figure 3.3: The profile of the first pulse

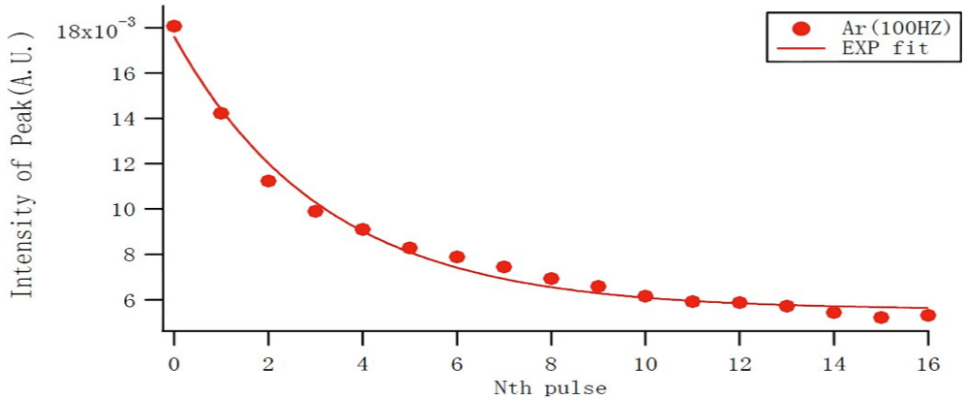

Figure 3.4: The intensity of each pulse in the train

The velocity of the slowed beam is related to the rotation frequency of the nozzle as shown in figure 3.5. As the rotation frequency increased, the TOF peak shifted to a later time. The inlet backing pressure was $3bar$, and valve opening time was $450\mu s$. The TOF measurements were fitted by the following equation 3.1 from[35]:

$$D(t) = \frac{C}{t}(\frac{L}{t} - V_{rot})e^{-(\frac{\frac{L}{t}-V}{\Delta v})^2} \tag{3.1}$$

where C is the total flux intensity, L is the flight distance, V_{rot} is the rotation velocity of nozzle with negative sign indicating slowing, Δv represents the velocity spread(full width at half maximum), V is the effective velocity of the beam in the laboratory frame.

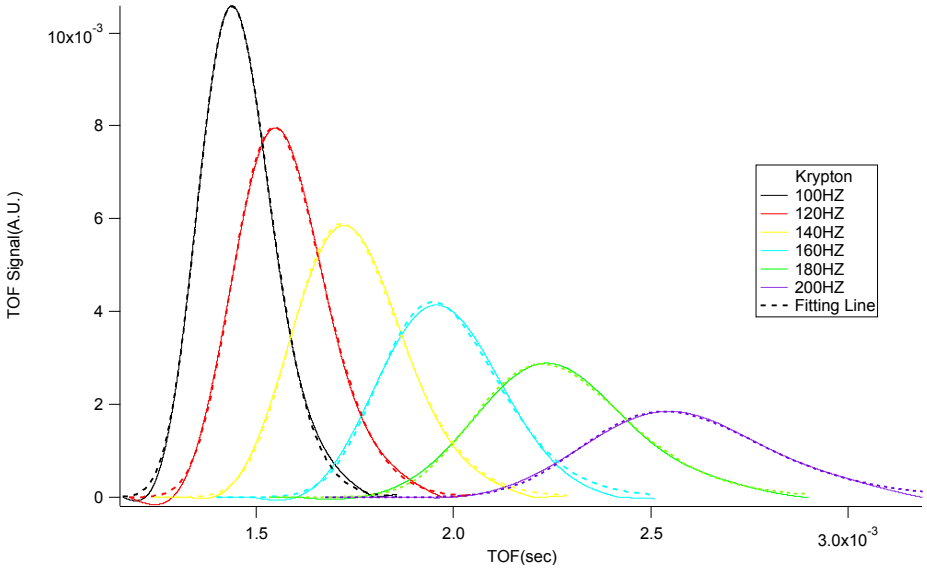

Figure 3.5: The krypton TOF with different rotation frequencies

The beam velocity was slowed down from about $380m/s$ to about $140m/s$ as shown in figure 3.6. The velocity of the beam was fitted with a straight line, which matched the expectation as predicted by V=X-V_{rot}.

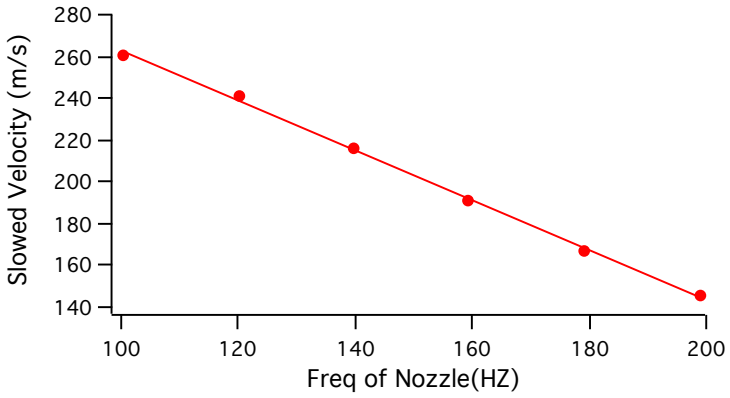

Figure 3.6: The slowed beam velocity with different rotation frequencies

One interesting point is that the supersonic expansion velocity of krypton at room temperature is supposed to be about $400m/s$, while the initial velocity of the krypton beam shown in figure 3.7 was about $380m/s$. One explanation about this phenomenon was the detector RGA's response time delayed the real arrival time, which resulted in slower beam velocities as we saw.

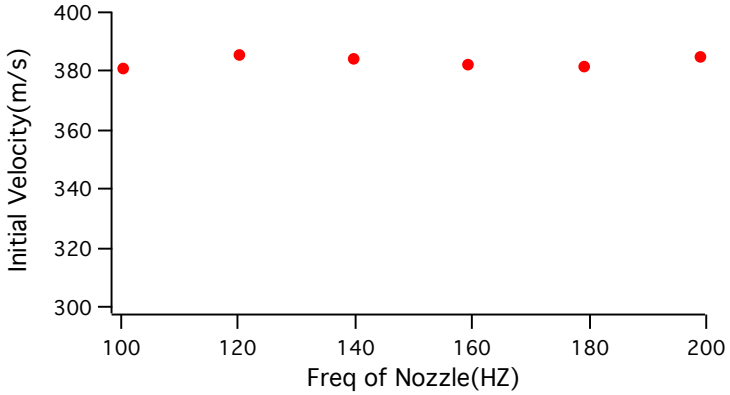

Figure 3.7: The krypton beam initial velocity with different rotation frequencies

Due to the centrifugal effect of rotating the nozzle, the pressure at the tip of the nozzle is higher than the inlet backing pressure. This effect becomes

more significant when increasing the rotation frequency. The other issue is that the pressure change will directly change the longitudinal temperature of the molecular beam, which is related to velocity spread by equation 3.2

$$\Delta v = (2k_b T_0/m)^{1/2}(T_{||}/T_0)^{1/2} \tag{3.2}$$

where k_b is the boltzmann constant, m is the particle mass, T_0 is the backing enviroment temperature, $T_{||}$ is the longitudinal temperature.

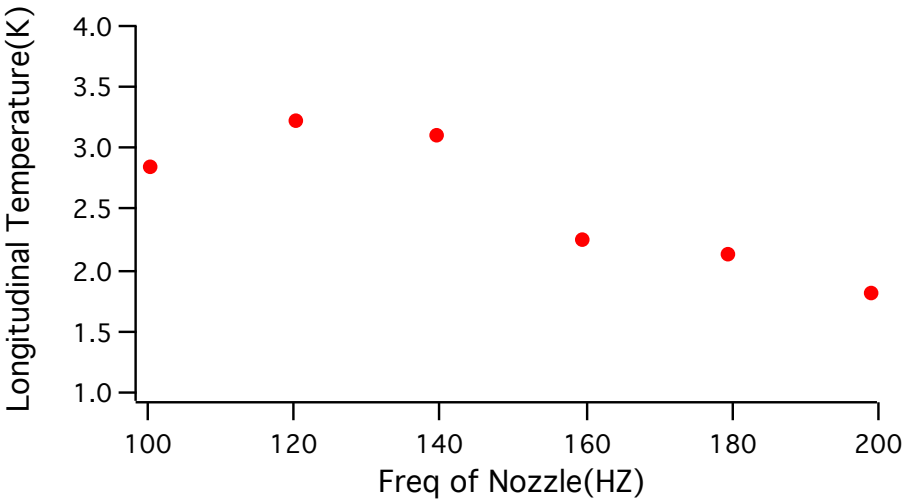

Figure 3.8: The krypton beam longitudinal temperature with different rotation frequencies

According to figure 3.8, the longitudinal temperature of krypton beam dropped when increasing the rotation speed. The reason was that the pressure P_0 at the tip of the nozzle increased due to the centrifugal effect described by equation 3.3[35]

$$\frac{P_0}{P_{in}} = exp[mV_{rot}^2/(2k_B T_0)] \tag{3.3}$$

where P_0 represents the pressure at the tip of the nozzle, P_{in} is the inlet backing pressure, m is the mass, V_{rot} is the velocity of the nozzle tip

The pressure would increased exponentially when increasing the rotation frequency as illustrated in 3.9. Supersonic expansion with a higher pressure at the tip of the nozzle cooled the internal temperature of the beam by about a factor of two.

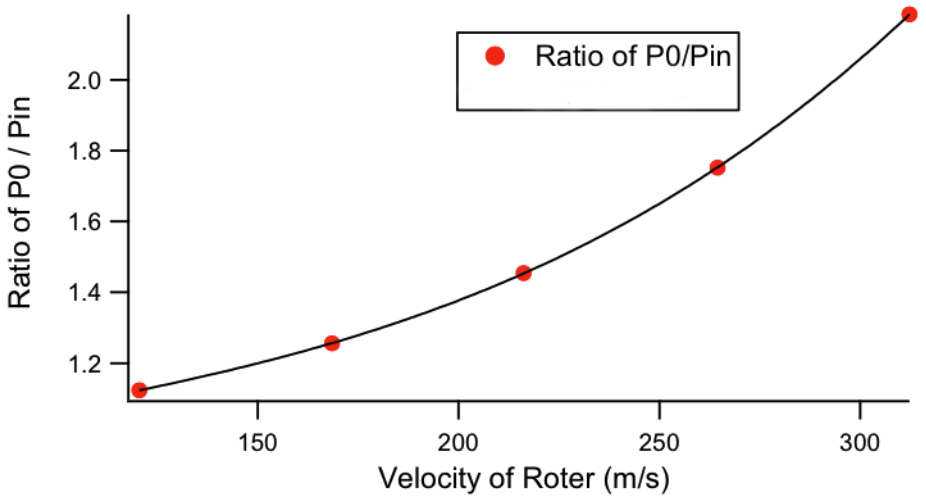

Figure 3.9: The calculated centrifugal effect on enhancement of pressure at the nozzle tip

The valve opening time is another factor which affects the longitudinal temperature besides pressure. Basically, if the valve opening time was longer, more gas went into the nozzle, and a higher pressure was obtained inside. This effect was proved by slowing the oxygen beam seeded in argon as shown in figure 3.10.

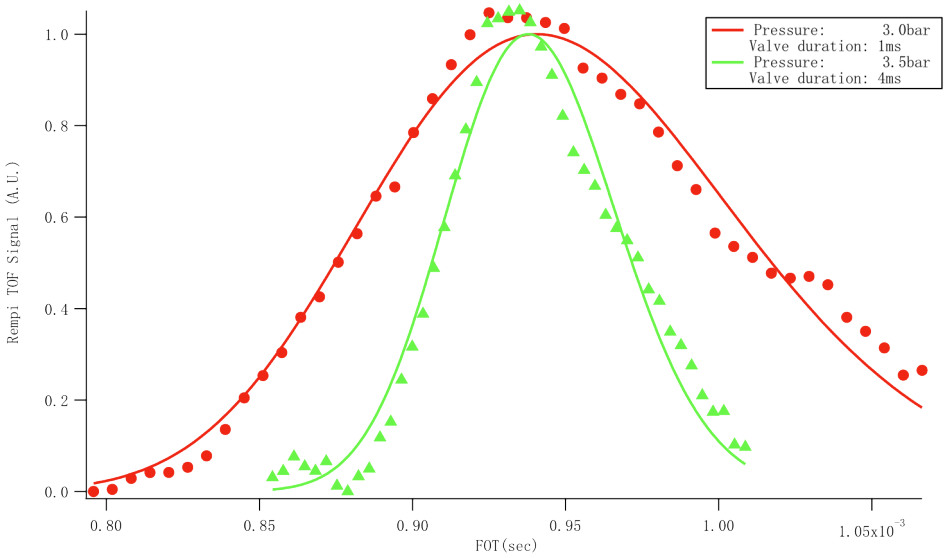

Figure 3.10: TOF measurements of slowed oxygen beams seeded in argon at a rotation frequency of $100Hz$

The longitudinal temperatures were about $4.5K$ and $1K$, corresponding to the red and green curves respectively. The longer opening time mainly contributed the lower longitudinal temperature.

Chapter 4

The microwave lens effect on polarized polyatomic molecular beams

In this chapter, we will demonstrate a MW lens effect for the J=0 rotational ground state of cold polyatomic beams, including CH_3CN and CD_3CN, created by the CRN. In order to observe any effect induced by the dipole force, precooling is necessary since the potential depth that the electromagnetic fields can generate is at most $1K$. For the true rotational ground state, precooling has to be achieved without using a static field according to Earnshaw's theorem. In this study, slowed CH_3CN and CD_3CN beams created by the CRN were introduced into a waveguide MW cavity, in which a TM_{01p} or TE_{11p} mode MW standing wave nearly resonant to the $|J, K\rangle = |1, 0\rangle \rightarrow |0, 0\rangle$ pure rotational transition was maintained. We have observed a difference in the number of molecules exiting the cavity by changing the condition of the MW standing wave such as the ON-duration time, the field strength and the detuning frequency, which indicated that the translational motion of a cold polyatomic beam in the J=0 rotational state was successfully influenced by the MW dipole force.

4.1 The AC Stark shift

The microwave lens effect we observed is due to the AC Stark shift associated with a molecular rotational transition. In our work, the discussion is confined to the effect of the MW field on two rotational states, $|J, K\rangle = |1, 0\rangle$ and $|0, 0\rangle$ of CH_3CN and CD_3CN. A linearly polarized electric field is built in the MW cavity. For dipole transitions induced by linearly polarized radiation, the optical selection rule of $\Delta J = \pm 1$, $\Delta K = 0$, and $\Delta M = 0$ applies for symmetric top molecules. Therefore, $|1, 0, 0\rangle$ is the only state that is accessible from the ground $|0, 0, 0\rangle$ rotational state by one photon transition. The total Hamiltonian of the system is given by $\widehat{H} = \widehat{H}_{rot} + \widehat{H}'$,

where $\widehat{H}' = -\boldsymbol{\mu} \cdot \boldsymbol{E}$ is the interaction between the electric dipole moment $\boldsymbol{\mu}$ of the molecule and the electric field $\boldsymbol{E}$. According to the dressed state formalism, the Hamiltonian matrix between the two basis sets $|0,0,0\rangle|\bar{n}+1\rangle$ and $|1,0,0\rangle|\bar{n}\rangle$ for linearly polarized radiation is approximated by

$$H = \begin{pmatrix} (\bar{n}+1)hv & \frac{1}{2}\varepsilon\mu_{10} \\ \frac{1}{2}\varepsilon\mu_{10} & 2B + \bar{n}hv \end{pmatrix} \tag{4.1}$$

where $\varepsilon = |\boldsymbol{E}|$ is the electric field amplitude, $\bar{n}$ is the number of photons in the field, hv is the photon energy with frequency of v and μ_{10} is the transition dipole moment between the resonant states, $|1,0,0\rangle$ and $|0,0,0\rangle$. For CH_3CN, $\mu_{10} = \langle 100|\mu|000\rangle = \mu_{10}\langle 100|cos\theta|000\rangle = 3.92/\sqrt{3} = 2.26debye$. For CD_3CN, $\mu_{10} = 3.31/\sqrt{3} = 1.91debye$. By diagonalizing the Hamiltonian matrix for the two-state model given in 4.1, the energy shift for the $|0,0,0\rangle$ state by the AC Stark effect is found to be

$$\Delta U_{000} = -\frac{\delta}{2} \pm \frac{1}{2}\sqrt{\delta^2 + \varepsilon^2{\mu_{10}}^2} \tag{4.2}$$

The energy shift of $|1,0,0\rangle$ state is

$$\Delta U_{100} = +\frac{\delta}{2} \mp \frac{1}{2}\sqrt{\delta^2 + \varepsilon^2{\mu_{10}}^2} \tag{4.3}$$

where $\delta = h(v - v_{10})$ is the detuning when the MW radiation frequency is v and the resonant transition frequency between the $|0,0,0\rangle$ and $|1,0,0\rangle$ states is $v_{10} = 2B/h$. The upper sign is for the blue detuning $\delta > 0$ case, and the lower sign is for the red detuning $\delta < 0$ case.

4.2 The electromagnetic field resonant mode spectrum in the microwave cavity

We established TM_{01p} and TE_{11p} mode electric fields in the microwave cavity. The index p denotes the number of nodes in the longitudinal direction of the cavity. These two different series of modes provide a linearly polarized radiation.

4.2.1 The TM_{01p} field and induced AC Stark dipole force distribution

The distribution of the electric field of TM_{01p} modes in a cylindrical cavity is completely concentric. The azimuthal component, E_θ, is zero. The

longitudinal component of electric field along central axis direction E_z, and radial component E_r, in cylindrical coordinates with the domain ($0 \leq z \leq L, 0 \leq r \leq a, 0 \leq \theta \leq 2\pi$) are given by

$$E_z = \varepsilon_0 J_0(\frac{x_{01} r}{a}) cos(kz) \tag{4.4}$$

and

$$E_r = \varepsilon_0 \frac{ka}{x_{01}} J_1(\frac{x_{01} r}{a}) sin(kz) \tag{4.5}$$

where a is the inner radius of cylindrical cavity, $6.29mm$, L is the length, $400mm$, ε_0 is the magnitude of the electric field, $k = p\pi/L$, $J_i(x)$ is the i-th order Bessel function of the first kind, $x_{01} = 2.4048$ is the first zero of $J_0(x)$ modes.

TM_{01p} modes in a cylindrical cavity have a concentric radial electric field distribution, and are ideal for demonstration of the lens effect of a molecular beam. The translational motion of the beam is affected by the AC dipole force, $\boldsymbol{F}$, given by $\boldsymbol{F} = -\nabla(\Delta U_{000})$, where ΔU_{000} is the energy shift given in equation 4.2. Since $a/L \ll 1$, the approximation of the dipole force distribution at a postion (r, z) in our cavity is:

$$F_r(r,z) = -\frac{\partial \Delta U_{000}}{\partial r} \approx \pm \frac{\mu_{10}^2 \varepsilon_0^2 x_{01}}{2a\sqrt{\delta^2 + E_z^2 \mu_{10}^2}} J_0(\frac{x_{01} r}{a}) J_1(\frac{x_{01} r}{a}) cos^2(kz) \tag{4.6}$$

The upper sign is for $\delta > 0$(blue detuning), and the lower sign is for $\delta < 0$(red detuning). For a red-detuned MW frequency, there is always a force towards the centric axis of the cavity.

The electric field distribution is as shown in figure 4.1. The scale of the radial direction, r, is exaggerated relative to the longitudinal direction, z.

The force distribution is as shown in figure 4.2. The magnitude of the radial component of the force F_r, is for the$|0, 0, 0\rangle$ state.

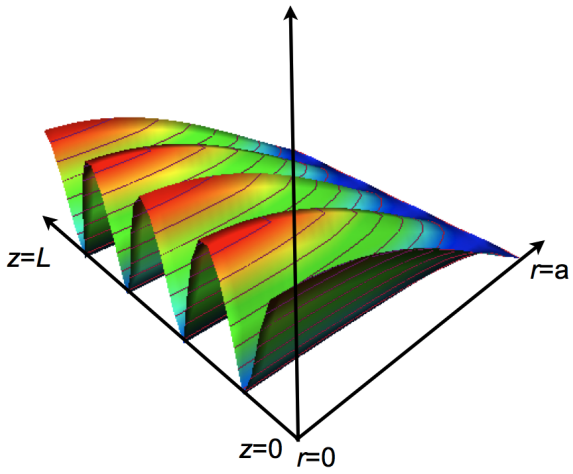

Figure 4.1: TM_{014} mode electric field distribution

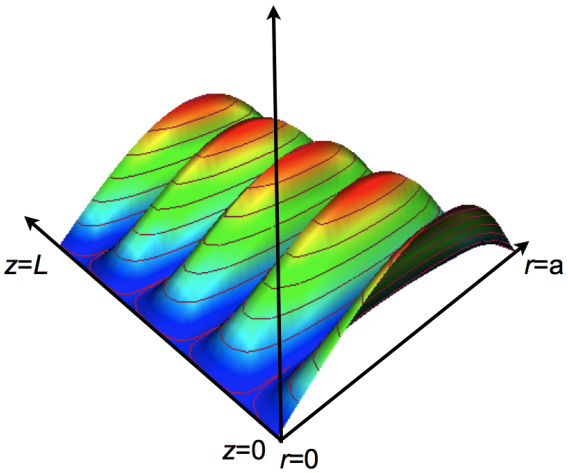

Figure 4.2: TM_{014} mode AC dipole force distribution

4.2.2 The TE_{11p} field and induced AC Stark dipole force distribution

Compared to TM_{01p} modes, which provide a two-dimensional radial confinement harmonic potential for HFS states, the TE_{11p} modes provide a three-dimensional trapping potential for HFS states at every antinode[42], which can be used for deceleration applications in the future. Here we present the electric field distribution of TE_{112} mode in y-z plane.

The electric field component along longitudinal direction E_z is 0, while the azimuthal component E_θ and radial component E_r are given by

$$E_r = E_0 \frac{J_1(x_{11}^{'} r/a)}{x_{11}^{'} r/a} sin\theta sin(kz) \tag{4.7}$$

and

$$E_\theta = E_0[J_0(\frac{x_{11}^{'} r}{a}) - \frac{J_1(\frac{x_{11}^{'} r}{a})}{\frac{x_{11}^{'} r}{a}}]cos\theta sin(kz) \tag{4.8}$$

where $x_{11}^{'}$ is 1.8412. According to $\boldsymbol{F} = -\nabla(\Delta U_{000})$, where $\Delta U_0 00$ is the AC Stark energy shift, each component of dipole force is given by

$$\begin{aligned} F_r = \pm\frac{1}{2}\frac{\mu_{10}^2 E_0^2 sin^2(kz)}{\sqrt{\delta^2 + (\vec{E}_r^2 + \vec{E}_\theta^2)\mu_{10}^2}}\{J_0^2(\frac{x_{11} r}{a})/r + J_1^2(\frac{x_{11}^{'} r}{a})[\frac{2a^2}{(x_{11}^{'})^2 r^3} - \frac{cos^2\theta}{r}] \\ + J_0(\frac{x_{11}^{'} r}{a}) J_1(\frac{x_{11}^{'} r}{a})[\frac{x_{11}^{'}}{a} cos^2\theta - \frac{a}{x_{11}^{'} r^2}(1 + 2cos^2\theta)]\} \end{aligned} \tag{4.9}$$

$$F_\theta = (-\frac{1}{r}) \cdot \pm\frac{1}{2}\frac{\mu_{10}^2 E_0^2 sin^2(kz) sin\theta cos\theta}{\sqrt{\delta^2 + (\vec{E}_r^2 + \vec{E}_\theta^2)\mu_{10}^2}}[\frac{2J_1(\frac{x_{11}^{'} r}{a})}{\frac{x_{11}^{'} r}{a}} - J_0(\frac{x_{11}^{'} r}{a})] J_0(\frac{x_{11}^{'} r}{a}) \tag{4.10}$$

$$\begin{aligned} F_z = \mp\frac{1}{2}\frac{\mu_{10}^2}{\sqrt{\delta^2 + (\vec{E}_r^2 + \vec{E}_\theta^2)\mu_{10}^2}}\{\vec{E}_r[E_0 k \frac{J_1(\frac{x_{11}^{'} r}{a})}{\frac{x_{11}^{'} r}{a}} sin\theta cos(kz)] \\ + \vec{E}_\theta[E_0 k[J_0(\frac{x_{11}^{'} r}{a}) - \frac{J_1(\frac{x_{11}^{'} r}{a})}{\frac{x_{11}^{'} r}{a}}]cos\theta\cos(kz)]\} \end{aligned} \tag{4.11}$$

By projecting the cylindrical coordinates onto Cartesian coordinates, the forces along x-direction and y-direction are derived as:

$$\begin{aligned} F_x &= F_r \cdot cos\theta - F_\theta \cdot sin\theta; \\ F_y &= F_r \cdot cos\theta + F_\theta \cdot sin\theta; \end{aligned} \tag{4.12}$$

The electric field distribution in y-z plane is as shown in figure 4.3

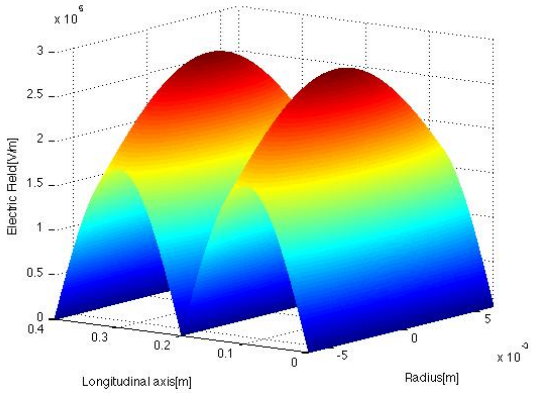

Figure 4.3: TE_{112} mode electric field distribution in y-z plane

The AC dipole force distribution in y-z plane is as shown in figure 4.4

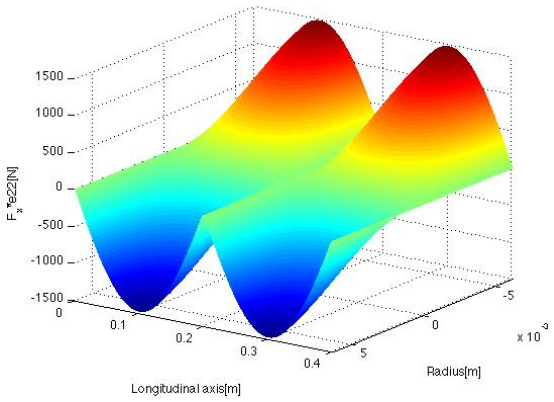

Figure 4.4: TE_{112} mode AC dipole force distribution in y-z plane

It is observed that the field and force distribution is non-centrosymmetric relative to the longitudinal axis. The electric field distribution in x-z plane is as shown in figure 4.5

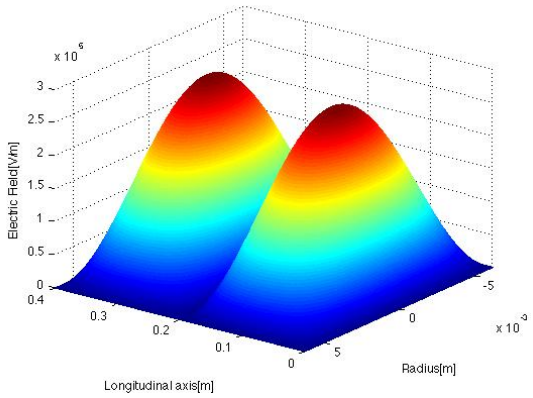

Figure 4.5: TE_{112} mode electric field distribution in x-z plane

and the AC dipole force distribution is as shown in figure 4.6

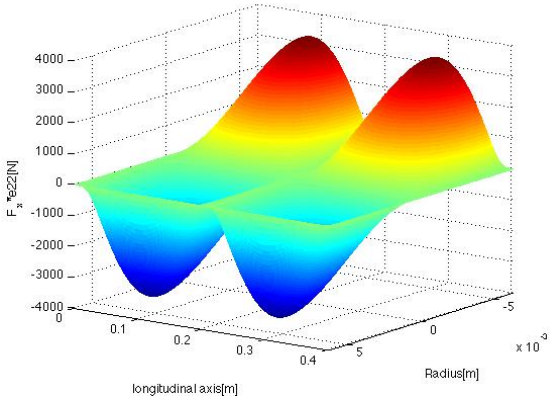

Figure 4.6: TE_{112} mode AC dipole force distribution in x-z plane

The electric field distribution in x-y plane, the cross section plane, is as shown in figure 4.7

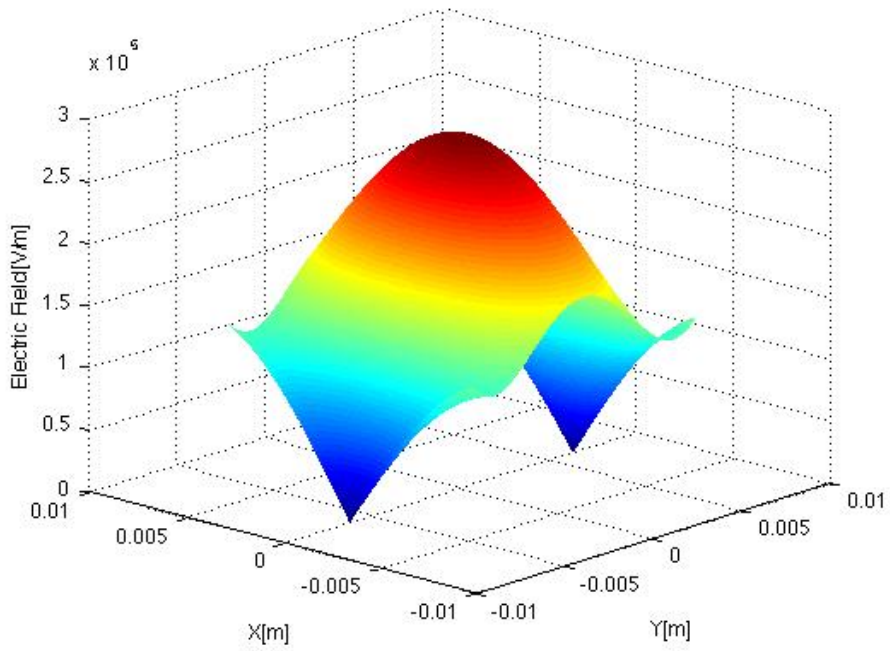

Figure 4.7: TE_{112} mode electric field distribution in x-y plane

4.3 The lens effect on CH_3CN beam by AC electric field in TM mode

4.3.1 The basic properties of CH_3CN

CH_3CN is a prolate symmetric top molecule with a permanent electric dipole moment of $\mu_0 = 3.92 debye$, which is linearly polarized, and a mass of $41u$. The structure is as shown in figure 4.8.

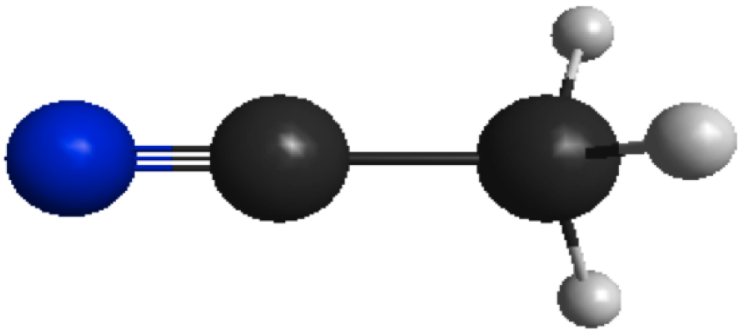

Figure 4.8: CH_3CN molecule structure

The black, white, blue balls represent carbon, hydrogen, nitrogen atoms, respectively. Its lowest pure rotational transition frequency$|J, K\rangle = |0, 0\rangle \rightarrow |1, 0\rangle$ is $18.398 GHz$.

The sample was introduced by bubbling in a stainless steel tube container at room temperature. The vapor pressure of CH_3CN is about $75 torr$ and the concentration when seeded in the krypton carrier gas is about 3.3% with backing pressure of $3 bar$.

Since the molecular beam was detected by a RGA detector, located about $6 cm$ behind the exit hole of the MW cavity, we calibrated the mass setting of the RGA very carefully. Krypton possesses isotopes of varying masses including ^{82}Kr(11.5%), ^{83}Kr(11.5%) and ^{84}Kr(58.0%). When these isotopes lose two electrons and Kr^{2+} is created, the charge-to-mass ratio is closely overlapping that of the target ion CH_3CN^+. The RGA mass spectrum of pure Kr supersonic beam is illustrated in figure 4.9

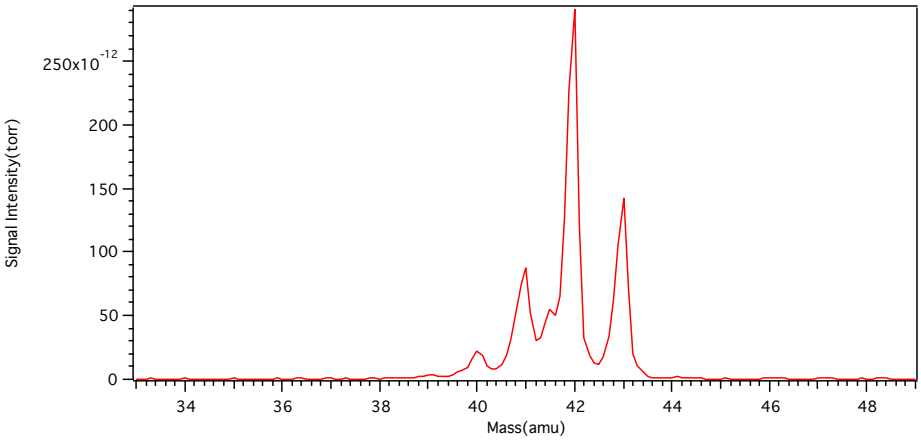

Figure 4.9: RGA mass spectrum of pure Kr

By detecting the pure Kr in the same condition, we confirmed that the signal of mass 41 produced by $^{82}Kr^{2+}$ and $^{83}Kr^{2+}$ were much weaker than that when CH_3CN seeded in the beam.

4.3.2 The populations of CH_3CN in $|0,0,0\rangle$ and $|1,0,0\rangle$ states

These two states follow the Boltzmann distribution:

$$\frac{N_i}{N} = \frac{g_i e^{-E_i/(k_B)T}}{\sum_i g_i e^{-E_i/(k_B T)}} \tag{4.13}$$

where k_B is the Boltzmann constant, T is rotational temperature, g_i is the degeneracy, N is the total number of particles, N_i is the number of particles in i-state and E_i is the energy level of i-state.

The energy levels are $E_i = \langle J,K,M|\widehat{H}_{rot}|J,K,M\rangle = BJ(J+1) + (A-B)K^2$. The rotational constants of CH_3CN are: A=158.3GHz and B=9.2GHz.

Each rotational state has a degeneracy of $2(2J+1)$ for $K \neq 0$ and $2J+1$ for $K = 0$. Due to the symmetrical configuration of the three protons, there are two spin modifications: $I = 3/2 ortho$-CH_3CN for $K = 3n$, and $I = 1/2 para$-CH_3CN for $K = 3n \pm 1$ (n is an integer) with a statistical ratio of 2 : 1.

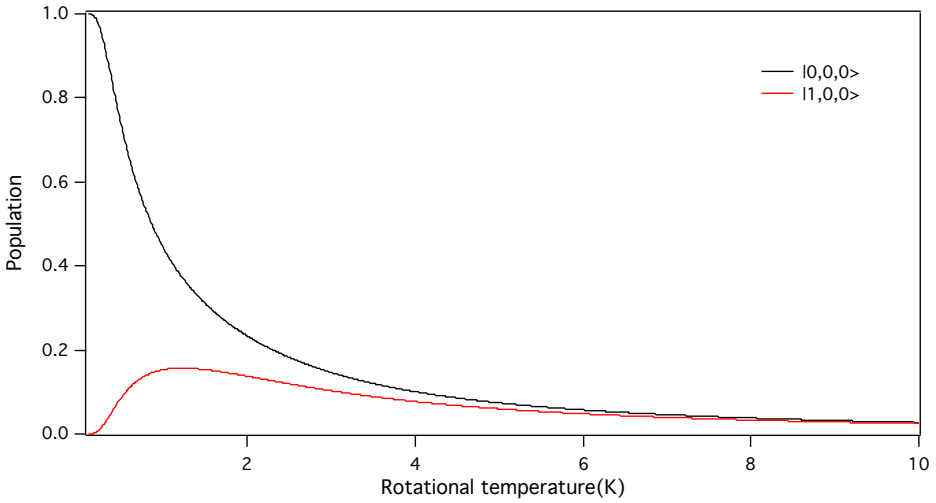

Figure 4.10: Populations of CH_3CN in $|0,0,0\rangle$ and $|1,0,0\rangle$ states

By considering this statistical ratio, the populations of CH_3CN in the $|J, K, M\rangle = |0, 0, 0\rangle$ and $|1, 0, 0\rangle$states are expected to be 5.7% and 4.8% respectively in molecular beam with a rotational temperature of $5K$.

4.3.3 The AC Stark shift of CH_3CN

The resonant transition frequency between $|0, 0, 0\rangle$ and $|1, 0, 0\rangle$ states are $v_{10} = 18.389GHz$. The transition dipole moment is $\mu = 2.26debye$. Assuming the electric field of about $460kV/m$, the detuning frequency of -$12MHz$ and $12MHz$, the AC Stark shift were depicted in figure 4.18. It's interesting that certain states such as $|0, 0, 0\rangle$ can be either HFS with red detuning or LFS with blue detuning. It applies to excited state such as $|1, 0, 0\rangle$ as well. The solid lines are blue detuning cases, and the dashed lines are red detuning cases. The AC Stark shift with these conditions is about $2GHz$

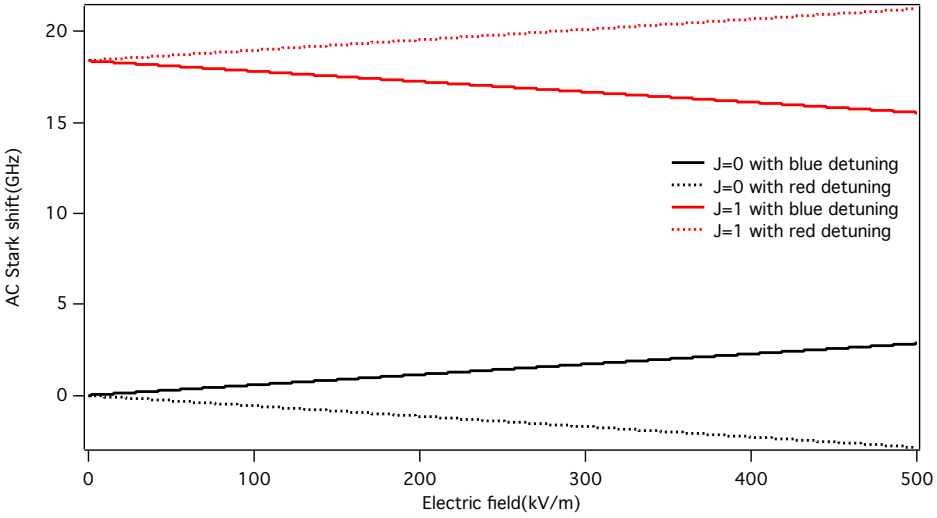

Figure 4.11: CH_3CN AC Stark shift with red and blue detunings of $12MHz$

4.3.4 The experimental results

From the equations 4.9, 4.10 and 4.11, we know that the motion of molecular beam, or the AC dipole force is dominated by the strength of the electric field and the detuning frequency, therefore these two factors' effects were explored in this section. In these experiments, in order to improve the vac-

uum of the microwave cavity and enhance the signal of the $J = 0$ ground state, we put a teflon disk at the center of the cavity to separate the cavity into two sections as mentioned. Most of the molecular beam would be blocked by the disk so that the vacuum in the second section would obtain an improvement to avoid high collision rates. By controlling the microwave generator, we can switch off the microwave in the first section or both of the sections.

Power-dependent experimental results

In this experiment, we applies the TM_{015} mode at $18.386GHz$ to the cavity, with a red detuning of $12MHz$. The loaded quality factor is about 10800. The MW power generated by the amplifier is about $5W$, while the actual power introduced into the cavity was about half of these values due to the loss of the coaxial cable. The electric field amplitude is about $123.7kV/m$ with consideration of the power loss. The signal intensity increase of CH_3CN beam is about 7% by height shown in figure 4.12

The blue trace shows the subtraction of the observed signals of CH_3CN seeded in Kr when MW is on and off in both sections, which is multiplied by a factor of 15.

By varying the input power generated by amplifier from $5W$ to $10W$, we find the observed RGA signal intensity increase is roughly doubled. The results are shown in figure 4.13, where the two traces are the subtractions of MW-ON signals and MW-OFF signals.

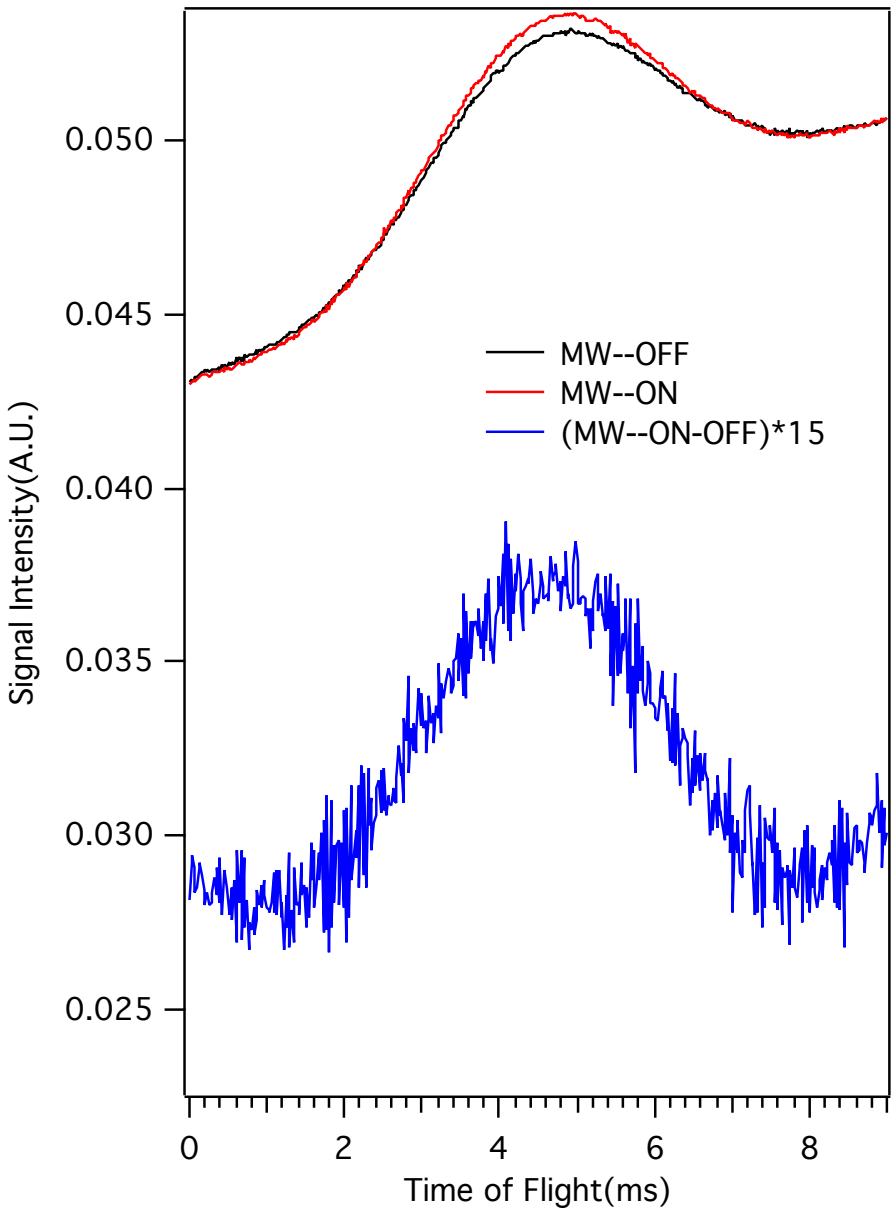

Figure 4.12: Focusing effect when applying red detuned microwave with power of $5W$

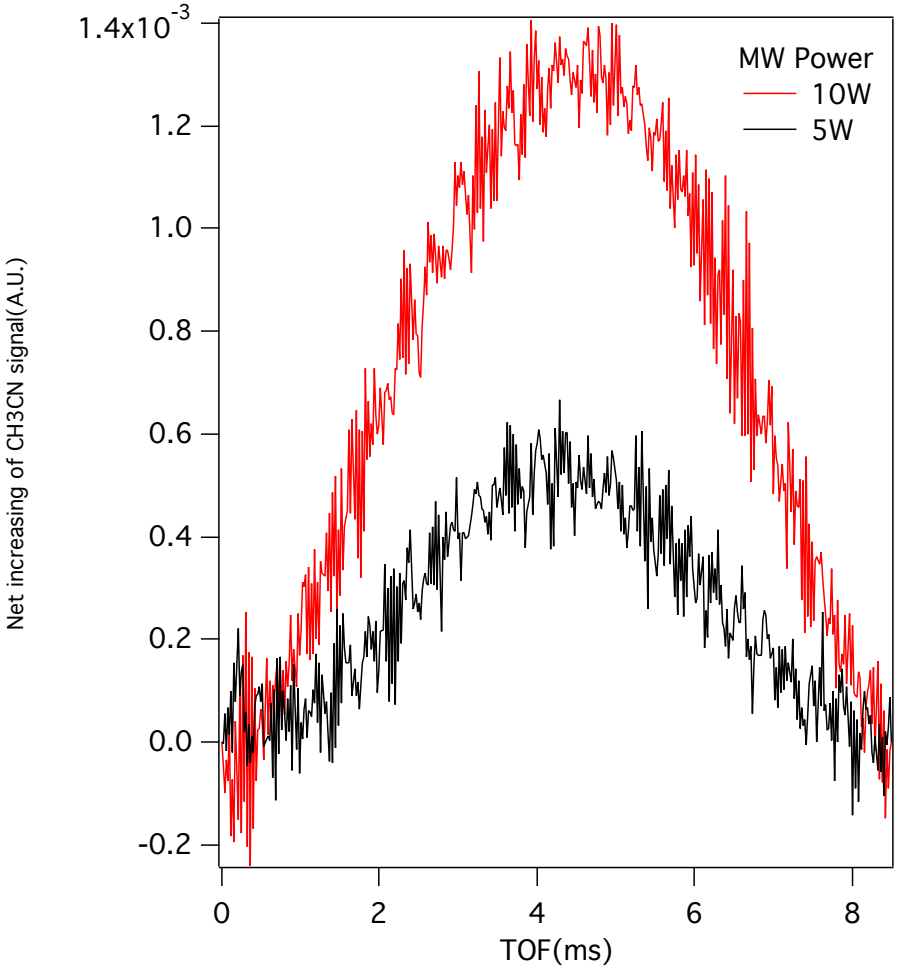

Figure 4.13: Focusing effect with different input powers

Experimental result with blue detuning

Figure 4.14 shows the CH_3CN signal when applying the TM_{016} MW field at $18.410GHz$. The loaded $Q\text{-}factor$ is $Q_L = 1.07 \times 10^4$. This frequency is slightly blue detuned from the resonant frequency of the target transition. With a blue detuned MW field, molecules in $|0,0,0\rangle$ state are deflected away from the central axis, while molecules in $|1,0,0\rangle$ is deflected towards the central axis. Since the populations of molecules in these two states are close to each other and the focusing effect is dominant, the intensity increase still shows up when applying blue detuned microwave.

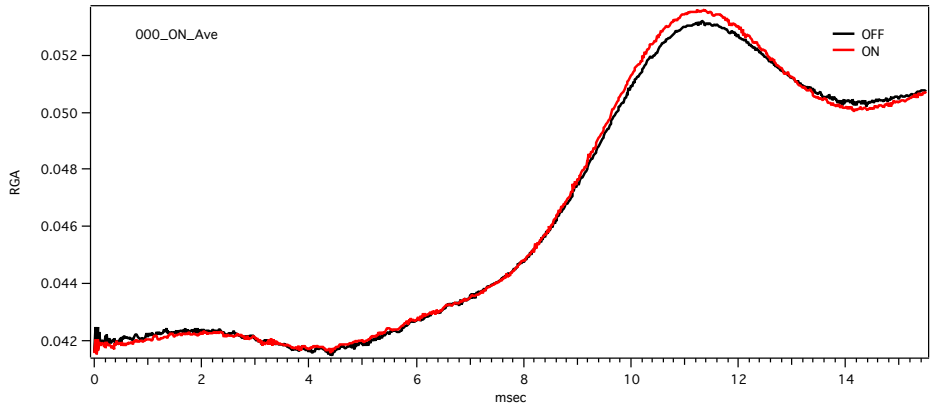

Figure 4.14: Focusing effect when applying blue detuning microwave

The signal increased by about 7% when the blue detuned microwave was switched on.

Experimental results of switching on one or both microwave sections

By changing the duration the microwave was applied on the molecular beam, we found the longer duration gave us stronger focusing effects. The microwave frequency was set to $18.343GHz(TM_{014})$. The power generated by the MW amplifier was $10W$ with a loaded Q-factor of $Q_L = 1.34 \times 10^4$

Figure 4.15 shows the result when switching off the microwave generator in both of sections. The signal intensity decreases by about 16%, while the signal intensity decreases by about 10% when switching off just in the first section as shown in figure 4.16. We subtracted the baseline caused by the background pressure change since we pulsed the molecular beam.

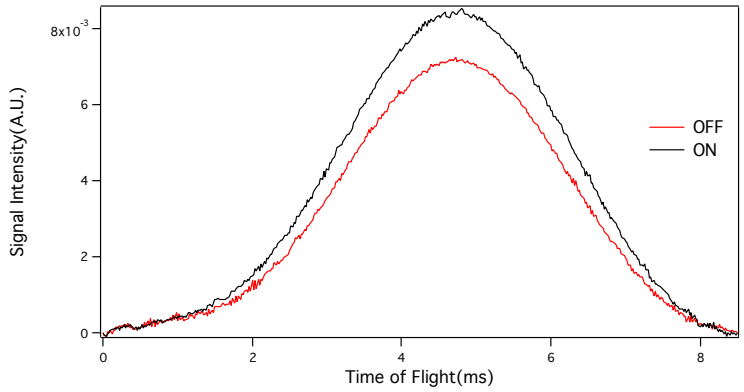

Figure 4.15: Focusing effect when switching off both of the sections

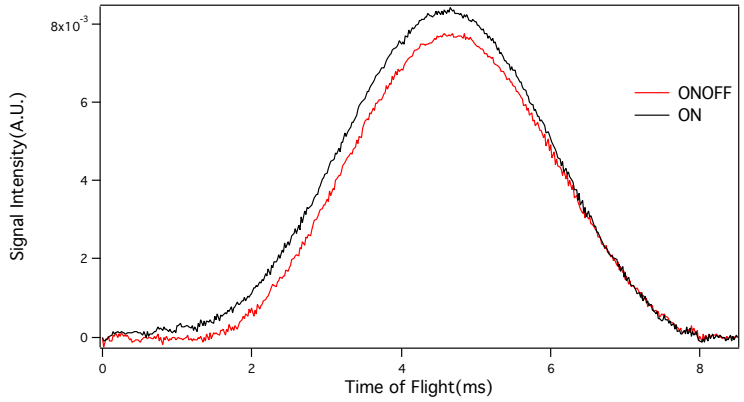

Figure 4.16: Focusing effect when switching off the first section

4.4 The lens effect on CD_3CN beam by AC electric field in TE mode

4.4.1 The basic properties of CD_3CN

The mass of CD_3CN is $44u$. It is a symmetric top molecule with the same structure as CH_3CN. The vapor pressure at room temperature is about 96 *torr*. The concentration when seeded in krypton carrier gas is about 4.2%. The energy level $\langle J, K, M|\widehat{H}_{rot}|J, K, M\rangle = BJ(J+1)+(A-B)K^2 - D_J J^2(J+1)^2 - D_{JK}J(J+1)K^2$. The rotational constants of CD_3CN are: A=$78.9GHz$, B=$7.9GHz$, D_J=$2.76KHz$ and D_{JK}=$110.7KHz$

The populations of molecules in $|0,0,0\rangle$ and $|1,0,0\rangle$ states are as shown in figure 4.17

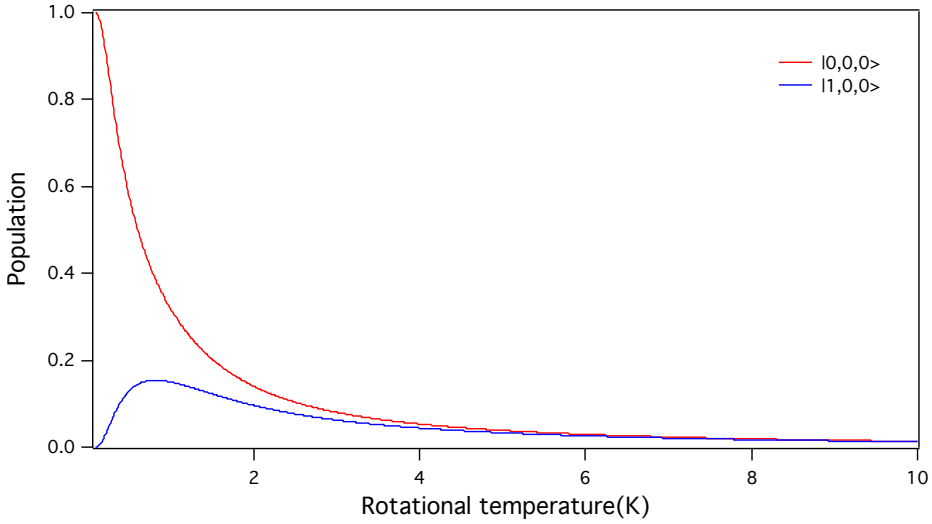

Figure 4.17: The populations of molecules in $|0,0,0\rangle$ and $|1,0,0\rangle$ states

Assuming a rotational temperature of $5K$, the populations of $|0,0,0\rangle$ and $|1,0,0\rangle$ states are about 3.9% and 3.3% respectively.

4.4.2 The AC Stark shift of CD_3CN

According to the equations 4.2 and 4.3, the AC Stark shifts of CD_3CN are as shown in figure 4.18

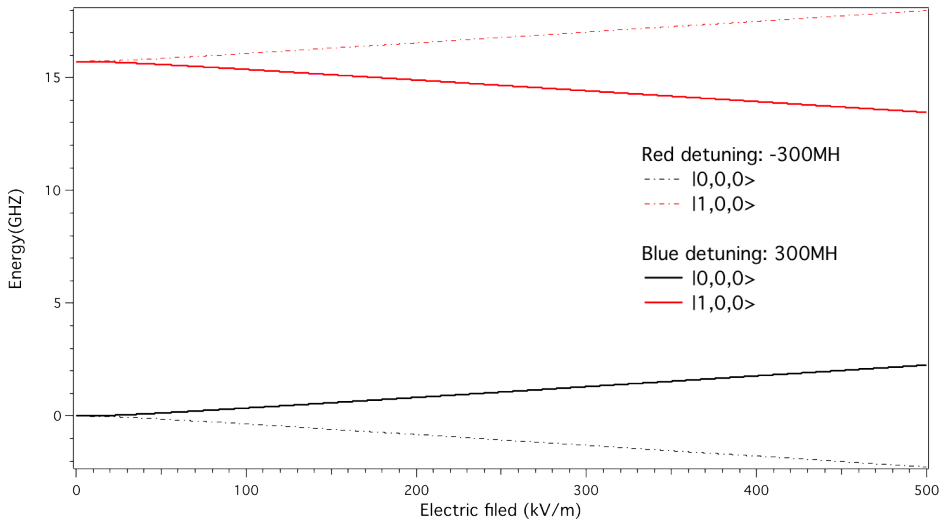

Figure 4.18: The AC Stark shift of CD_3CN

The resonant transition frequency between these two states is $v_{10} = 15.716GHz$. The transition dipole moment is $\mu = 1.91debye$. Assuming the electric field of about $460kV/m$, the detuning frequencies of -$300MHz$ and $300MHz$, the AC Stark shift is obtained in figure 4.18. The AC Stark shift with these conditions is about $2GHz$

4.4.3 The experimental and simulation results

The repetition time between pulses is $5s$ to maintain the high vacuum inside the system. The background pressure change during pulses in detection chamber is as shown in figure 4.19

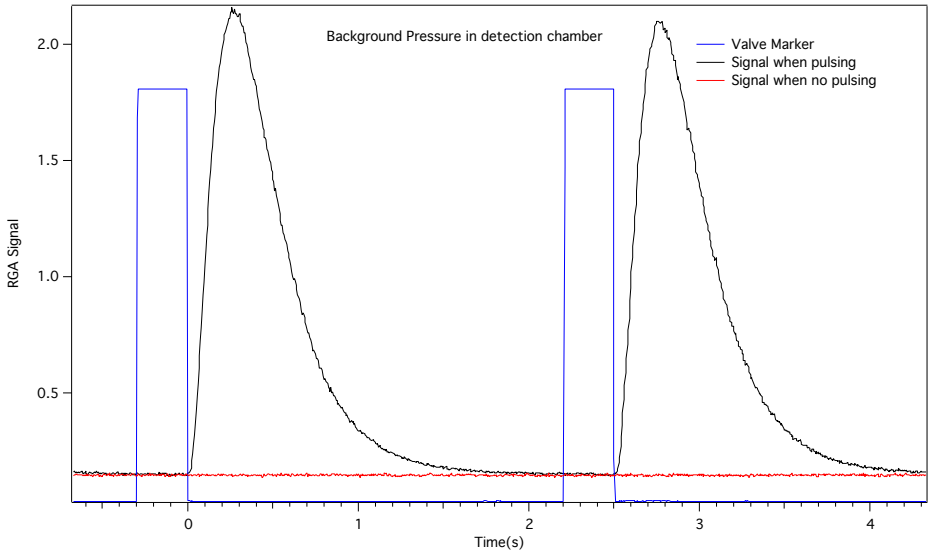

Figure 4.19: Background pressure fluctuation in detection chamber when pulsing

The background pressure recovered to original conditions after $2.5s$. However, considering the reading showed the pressure in the detection chamber, not in the microwave cavity, we lengthened the repetition time to $5s$ to make sure the vacuum inside the cavity restored properly since a large part of the molecular beam was blocked inside the cavity.

Power-dependent Experimental and simulation results

TM_{1118} at a frequency of 15.542 MHz was chosen for this experiment. The red detuning frequency was about $174MHz$. The amplifier type we used was a traveling-wave tube (TWT) amplifier. Due to nonlinearity features of the amplifier and the energy loss during transmission with the new antenna, we calibrated the output power after the TWT amplifier corresponding to different input power from microwave generator. The relation between the input power in units of dBm and the output power after the TWT in units of W is depicted in figure 4.20

According to equation 4.15 and 4.14[42], we can calculate the amplitude of the electric field in the microwave cavity once we know the power input into the cavity.

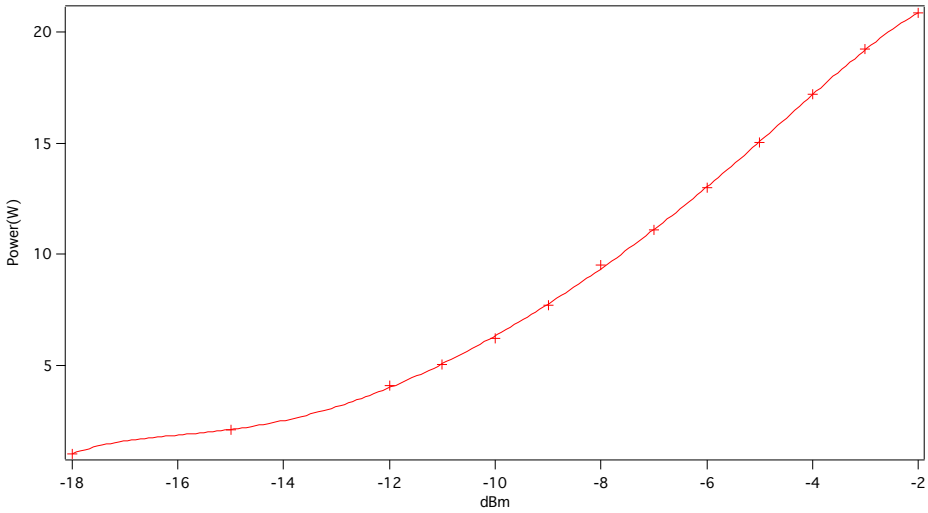

Figure 4.20: The calibration of output power after TWT amplifier

$$W = \frac{P_{in} Q_L}{\pi V} \tag{4.14}$$

$$W = 0.02984 \epsilon_0 E_0^2 V \tag{4.15}$$

where P_{in} is the power inputed into the cavity, Q_L is the loaded Q factor, E_0 is the amplitude of the electric field, V is the volume of the microwave cavity, and $\epsilon_0 = 8.8 \times 10^{-12} F/m$ is the permittivity.

For example, if the output power of the TWT amplifier is $7.7W$, the power loss after the antenna is 11% according to the parameters in the antenna manual. The actual input power into the microwave cavity is about $6.8W$. The dimension of the cavity is $400.0mm$ in length and $6.3mm$ in radius. Therefore the volume is about $50cm^3$. The Q_L is about 12000. The electric amplitude is $355kV/m$ for this case.

We varied the input power from $4W$ to $16.8W$, corresponding to a electric field of $256kV/m$ to $525kV/m$. The TOFs for several cases are as shown in figure 4.21

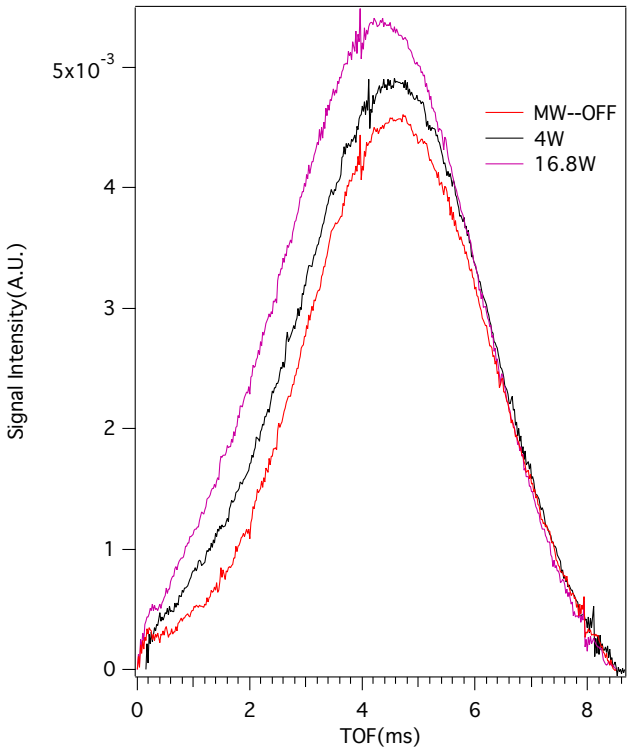

Figure 4.21: Experimental focusing effect with various input power

The longitudinal velocity of the CD_3CN beam created by the CRN was about $120m/s$ with velocity spread of about $\pm 20m/s$.

We noticed that the faster molecules were focused better than slower molecules. The main reason for this phenomenon is that slower ones are easier to over-focus.

The simulation results are as shown in figure 4.22. By assuming the rotational temperature of $5K$, the population ratio is about 1.15:1. The number of simulated molecules is 1×10^6 for each state and we added both of the TOFs together by ratio of 1.15:1.

The simulation results also showed that the peaks of the TOFs shifted to earlier time for higher microwave by fitting with Gaussian distribution. The TOF peak of $4W$ case appeared at $4.79ms$, while at $16.8W$ the peak shifted slightly earlier to $4.72ms$.

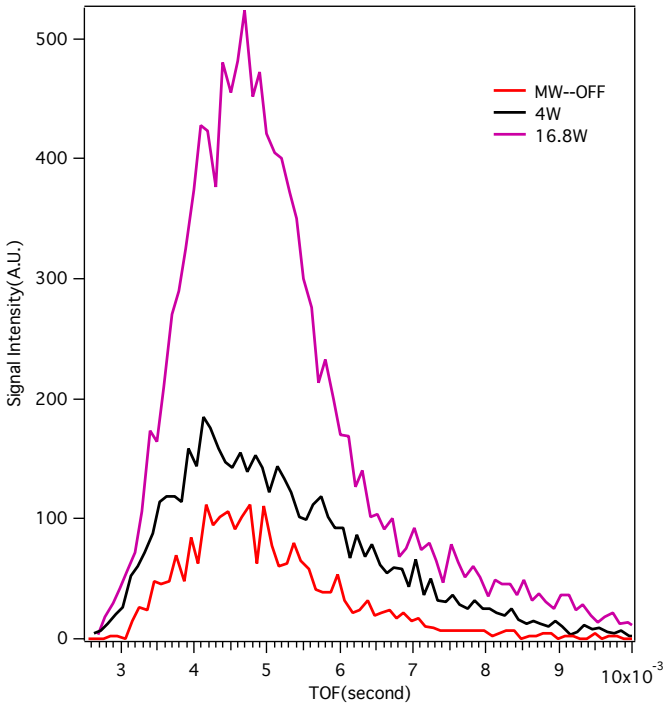

Figure 4.22: Simulated focusing effect with various input power

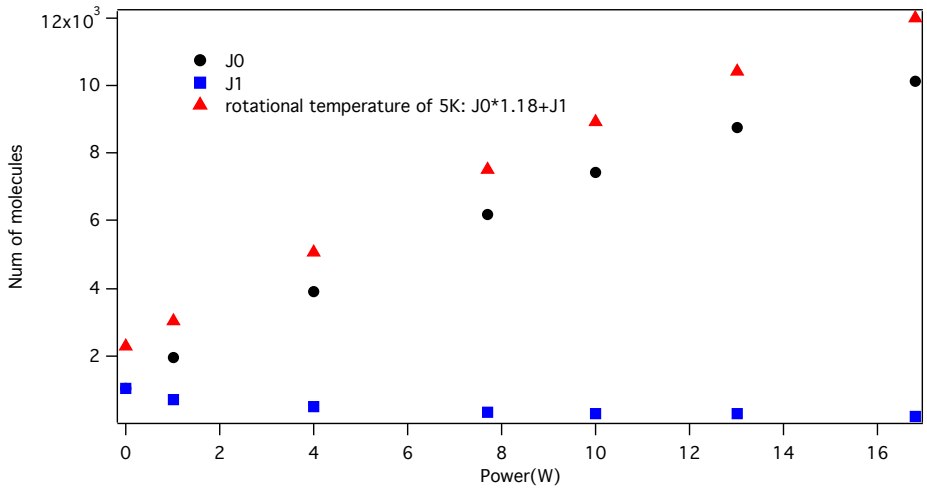

Figure 4.23: Simulated number of detected molecules with various power

We once expected the focusing effect was proportional to the input power or proportional to the square root of the power. However, as shown in figure 4.23, the number of detected $|0,0,0\rangle$ state molecules and $|1,0,0\rangle$ state molecules supported neither of these cases. Since the motion of molecules was complicated in the microwave cavity and the detected signal depended on the combination of them, the relationship between the focusing effect and the input power was mainly dominated by the focusing of $|0,0,0\rangle$ when we applied red detuning and that of $|1,0,0\rangle$ when we applied blue detuning.

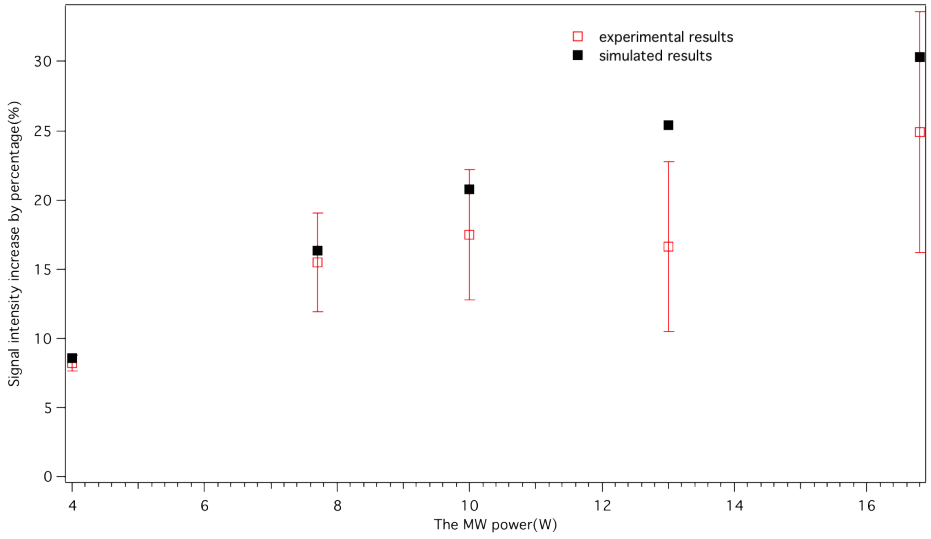

Figure 4.24: Simulated and experimental signal intensity increase by percentage

The average intensity increase was about 8% with $4W$ and 23% with $16.8W$. The red markers with error bars showed the experimental intensity increase by area when increasing input power. It was noticed that the intensity increase became saturated compared to the simulated black markers when applying higher power. Also the error bars were larger with higher power. One of the possibilities could be that collisions between the molecules and between molecule and cavity wall were more intense with higher power, which resulted in the saturation and larger error bar.

Detuning-dependent experimental and simulation results

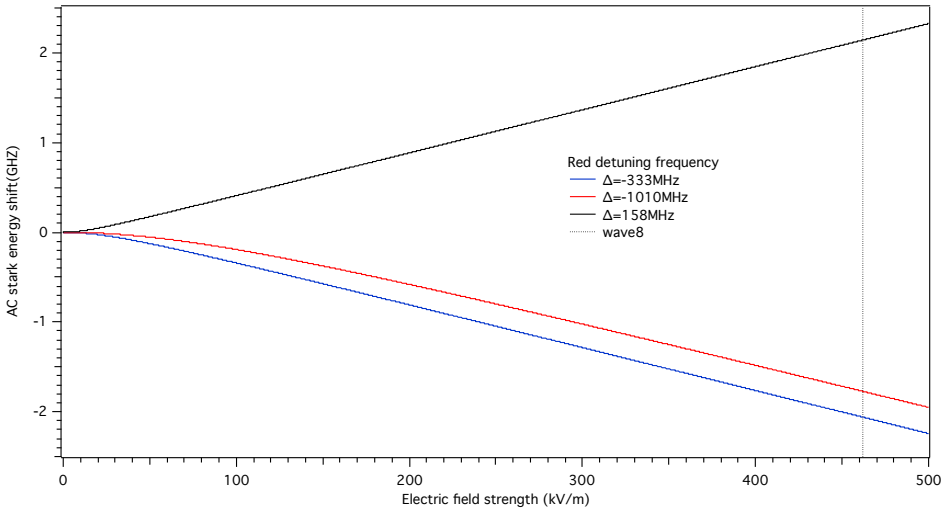

Figure 4.25: AC Stark shifts for different detunings

The input power we chose for detuning-experiments was $16.8W$, corresponding to an electric field with amplitude of about $462kV/m$ shown as dashed vertical line in figure 4.25. The AC Stark shift of red detuning of $333MHz$ was $2.0GHz$, that of red detuning of $1010MHz$ was $1.8GHz$, and that of blue detuning of $158MHz$ was $2.1GHz$. Even though the AC Stark shift depended on both the electric field and detuning frequency, the detuning frequency changes contributed much less than the electric field strength changes.

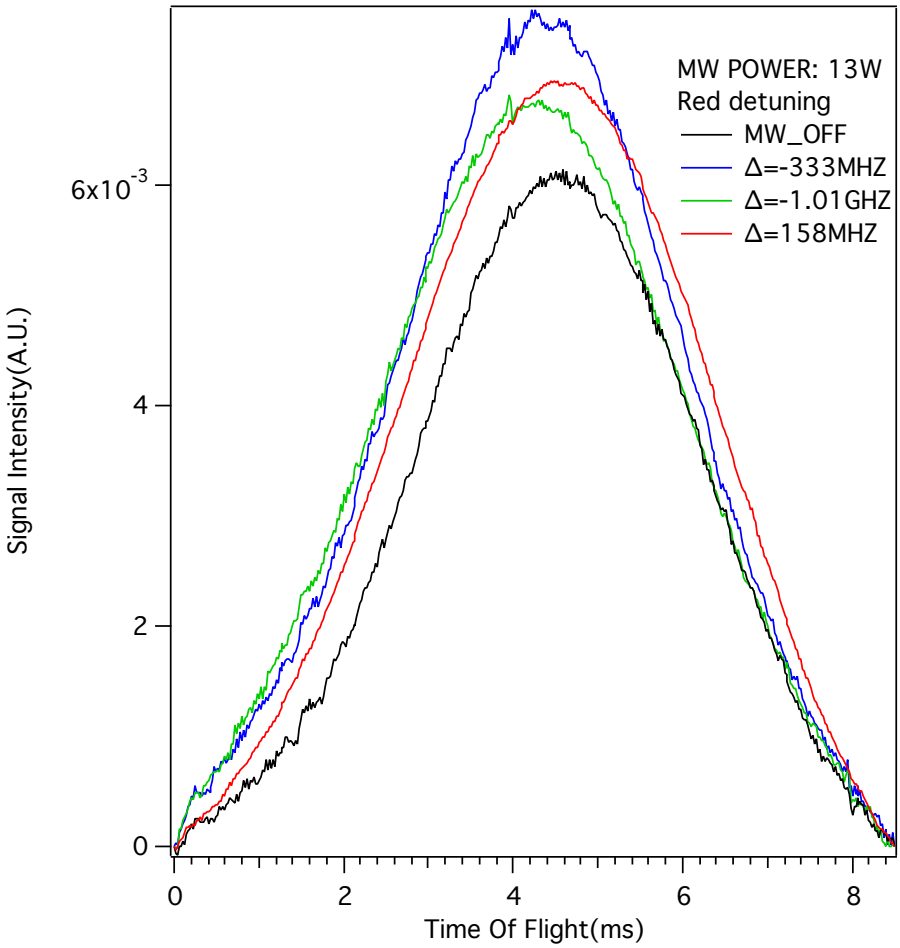

Figure 4.26: Focusing effect with various detuning

As mentioned above, the focusing effect dominated compared to the defocusing effect. Therefore, for both red and blue detuning experiments, we expected to see focusing of the molecular beam. Three different conditions were chosen for this experiments: two red detuning and one blue detuning. The red detuning of $333MHz$ gave about an 27% intensity increase, while the red detuning of $1010MHz$ gave about an 20% intensity increase instead. Smaller detuning gave us stronger lens effect. The very interesting observation is that even though $158MHz$ of blue detuning was closer to the transition frequency than $333MHz$ of red detuning, the focusing effect was

smaller for blue detuning. The signal intensity increased by 22%. The reason was that the population of $|0,0,0\rangle$ state was slightly larger than that of $|1,0,0\rangle$ state. Therefore, the focusing of $|1,0,0\rangle$ state contributed less when applying blue detuning, comparing to the focusing of $|0,0,0\rangle$ state when applying red detuning.

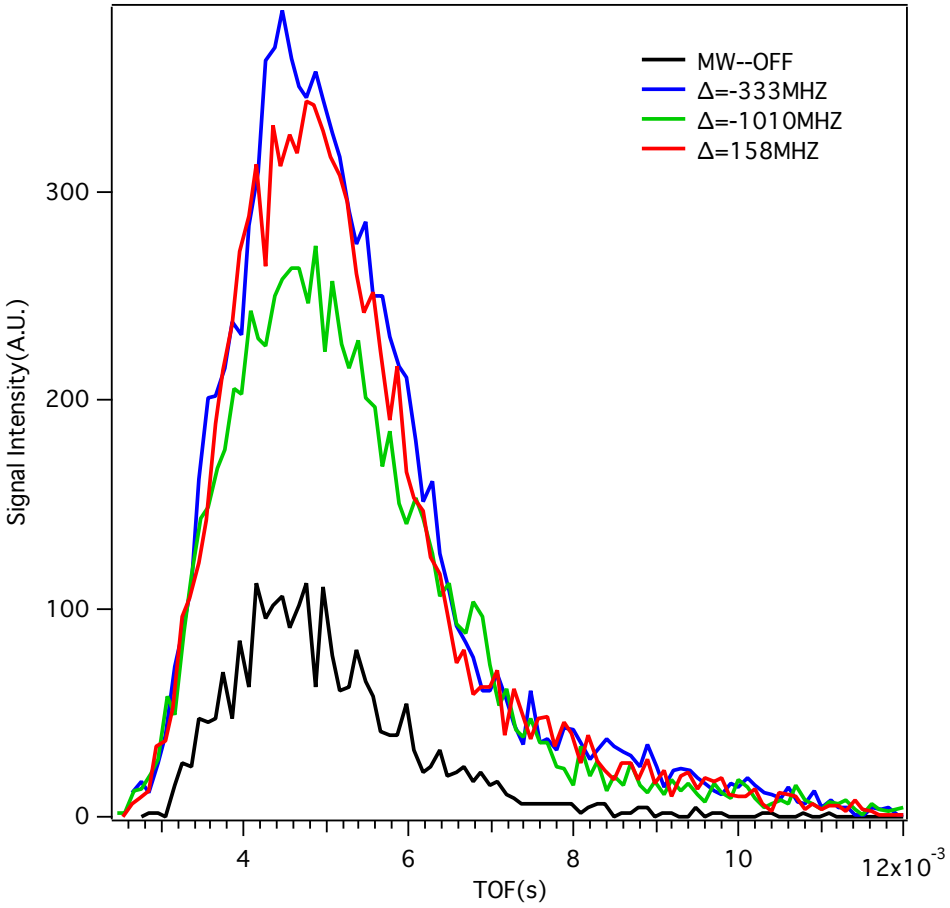

Figure 4.27: Simulated focusing effect with various detuning

The simulation results are as shown in figure 4.27, which matched with the experimental results very well. The blue detuning of $158MHz$ gave larger focusing than red detuning of $1010MHz$, and smaller than red detuning of $333MHz$.

4.5 Experimental lens effect demonstration of an acetone beam in TE mode

Besides CH_3CN and CD_3CN samples, We also conducted microwave lens experiments with molecules like acetone $CO(CH_3)_2$, which has more complicated molecular structure. Its two-state transition spectrum in the microwave range (around $15GHz$) is quite sophisticated because of the two-rotor structure resulting in large amount of degeneracies. Figure 4.28 shows a demonstration of the lens effect on an acetone beam.

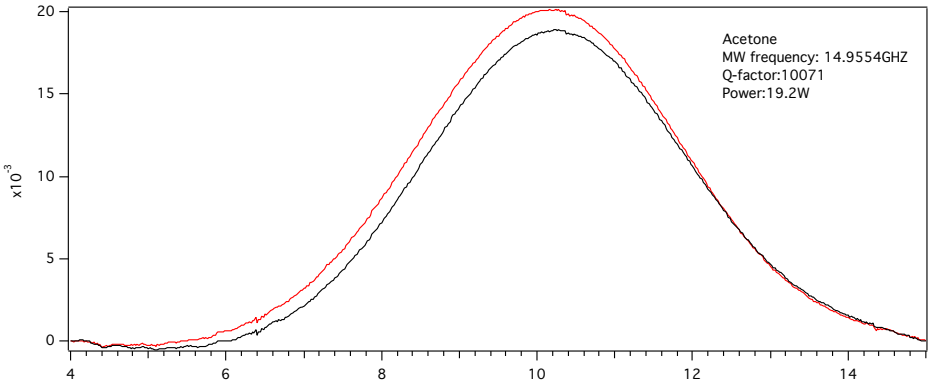

Figure 4.28: Lens effect on an acetone beam

Chapter 5

Conclusion and future work

In this thesis, we have presented our observations of the focusing effect on CH_3CN and CD_3CN molecular beams. The relation between the focusing effect and microwave power and frequency-detuning was explored. The beam intensity change due to our changes to experimental conditions proved that we successfully manipulated the motion of the beam. We found that the intensity of faster molecules in the beam increased more than that of slower molecules because the slower molecules experienced more time in the standing wave and were easily over-focused. We found the focusing effect saturated as we increased the power up to $16.8W$, which was mainly because most accessible molecules in the rotational ground states already succeed in exiting the microwave cavity. When applying the blue detuning to the molecular beam, we expected to see defocusing effect initially. However, we found that the focusing effect always appeared even with a blue detuning, which meant the focusing effect was dominant in these manipulation experiments. Since the RGA detector detected molecules in all states, the focusing of $J = 1$ state molecules not only compensated the defocusing of $J = 0$ state molecules, but also enhanced the total intensity of the molecular beam at the detector. This was confirmed by both experimental and simulation results.

Now, we are working on the construction of a half meter long superconducting cylindrical cavity coated by the lead-tin as shown in figure 5.1, for which we expect to achieve a $PQ\text{-}factor$ as high as 10^7 and a electric field with a strength of $2MV/m$ when cooled down to around $3K$. For a CH_3CN beam with an initial speed of $80m/s$, TE_{1150} with 50 nodes can succeed in decelerating the beam to a standstill.

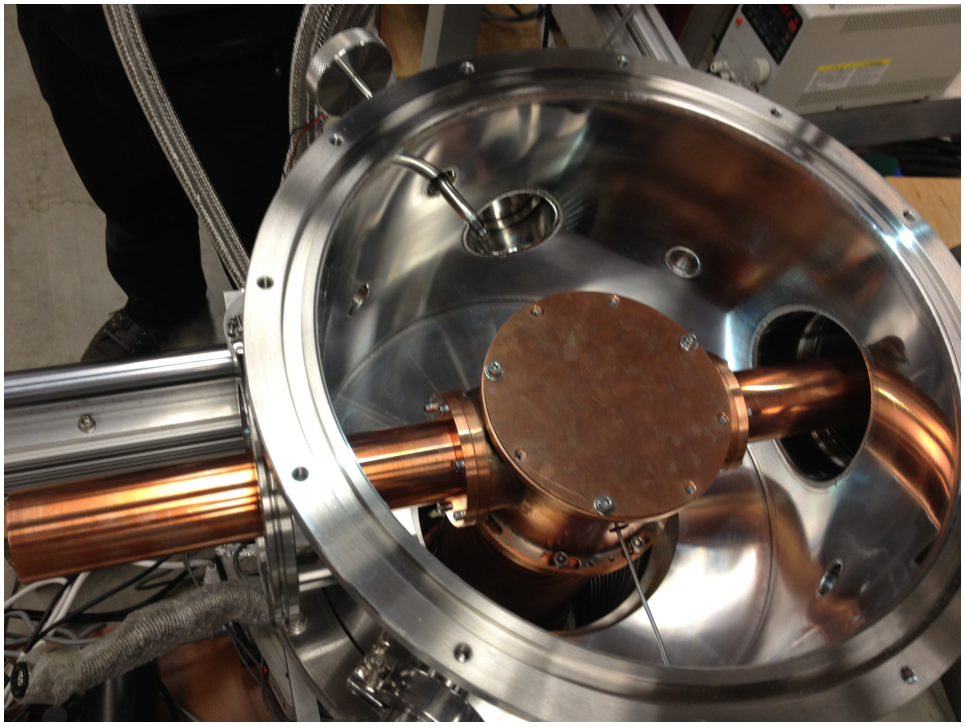

Figure 5.1: The superconducting microwave cavity attached to the cryocooler

Bibliography

[1] Steffen Spieler, Wei Zhong, Pavle Djuricanin, Omid Nourbakhsh, Ilja Gerhardt, Katsunari Enomoto, Frank Stienkemeier, and Takamasa Momose. Microwave lens effect for the J = 0 rotational state of CH3CN. *Molecular Physics*, 111:1823–1834, 2013.

[2] The 2012 nobel prize in physics - press release, July 2013.

[3] Lincoln D Carr, David DeMille, Roman V Krems, and Jun Ye. Cold and ultracold molecules: science, technology and applications. *New Journal of Physics*, 11:055049, 2009.

[4] Bretislav Friedrich and John M. Doyle. Why are cold molecules so hot? *ChemPhysChem*, 10:604 – 623, 2009.

[5] Cheng Chin, V V Flambaum, and M G Kozlov. Ultracold molecules: new probes on the variation of fundamental constants. *New Journal of Physics*, 11:055048, 2009.

[6] David W. Chandler and Kevin E. Strecker. The quest for cold and ultracold molecules. *ChemPhysChem*, 10:751 – 754, 2009.

[7] Deborah S. Jin and Jun Ye. Introduction to ultracold molecules: New frontiers in quantum and chemical physics. *Chemical Reviews*, 112:48014802, September 2012.

[8] Martin T. Bell and Timothy P. Softley. Ultracold molecules and ultracold chemistry. *Molecular Physics*, 107:99–132, 2009.

[9] Melanie Schnell and Gerard Meijer. Cold molecules: Preparation, applications, and challenges. *Angew. Chem. Int. Ed.*, 48:6010 – 6031, 2009.

[10] O Dulieu and C Gabbanini. The formation and interactions of cold and ultracold molecules: new challenges for interdisciplinary physics. *Reports on Progress in Physics*, 72:086401, 2009.

[11] S. Charles Doret, Colin B. Connolly, Wolfgang Ketterle, and John M. Doyle. Buffer-gas cooled bose-einstein condensate. *Physical Review Letters*, 103:103005, 2009.

[12] Goulven Quéméner and John L. Bohn. Strong dependence of ultracold chemical rates on electric dipole moments. *Physical Review A*, 81:022702, 2010.

[13] Qi Wei, Igor Lyuksyutov, and Dudley Herschbach. Merged-beams for slow molecular collision experiments. *The Journal of Chemical Physics*, 137:054202, 2012.

[14] Serge A. Krasnokutski and Friedrich Huisken. Ultra-low-temperature reactions of mg atoms with o2 molecules in helium droplets. *J. Phys. Chem. A*, 114:7292–7300, 2010.

[15] Zbigniew Idziaszek, Goulven Quéméner, John L. Bohn, and Paul S. Julienne. Simple quantum model of ultracold polar molecule collisions. *Physical Review A*, 82:020703(R), 2010.

[16] D M Kara, I J Smallman, J J Hudson, B E Sauern, M R Tarbutt, and E A Hinds. Measurement of the electron's electric dipole moment using ybf molecules: methods and data analysis. *New Journal of Physics*, 14:103051, 2012.

[17] J. J. Hope and M. K. Olsen. Quantum superchemistry: Dynamical quantum effects in coupled atomic and molecular bose-einstein condensates. *Physical Review Letters*, 86:3220, 2001.

[18] D. DeMille. Quantum computation with trapped polar molecules. *Physical Review Letters*, 88:067901, 2002.

[19] Application of lasers to ultra-cold atoms and molecules. *Comptes Rendus Physique*, 12:417–432, 2011.

[20] E. S. Shuman, J. F. Barry, and D. DeMille. Laser cooling of a diatomic molecule. *Nature*, 467:820–823, October 2010.

[21] Michał Tomza, Filip Pawłowski, Małgorzata Jeziorska, Christiane P. Koch, and Robert Moszynski. Formation of ultracold SrYb molecules in an optical lattice by photoassociation spectroscopy: theoretical prospects. *Phys. Chem. Chem. Phys.*, 13:18893–18904, 2011.

[22] Mihaela Vatasescu. Formation of cold molecules by shaping with light the short-range interaction between cold atoms: photoassociation with strong laser pulses. *Journal of Physics B: Atomic, Molecular and Optical Physics*, 42:165303, 2009.

[23] Hendrick L. Bethlem, Floris M. H. Crompvoets, Rienk T. Jongma, Sebastiaan Y. T. van de Meerakker, and Gerard Meijer. Deceleration and trapping of ammonia using time-varying electric fields. *Physical Review A*, 65:053416.

[24] Hendrick L. Bethlem, André J. A. van Roij, Rienk T. Jongma, and Gerard Meijer. Alternate gradient focusing and deceleration of a molecular beam. *Physical Review Letters*, 88:133003, 2002.

[25] M. R. Tarbutt, H. L. Bethlem, J. J. Hudson, V. L. Ryabov, V. A. Ryzhov, B. E. Sauer, G. Meijer, and E. A. Hinds. Slowing heavy, ground-state molecules using an alternating gradient decelerator. *Physical Review Letters*, 92:173002, 2004.

[26] Takamasa Momose, Yang Liu, Sida Zhou, Pavle Djuricanin, and David Carty. Manipulation of translational motion of methyl radicals by pulsed magnetic fields. *Phys. Chem. Chem. Phys*, 15:1772, 2013.

[27] Alisdair O. G. Wallis and Jeremy M. Hutson. Production of ultracold nh molecules by sympathetic cooling with mg. *Physical Review Letters*, 103:183201, 2009.

[28] P Barletta, J Tennyson, and P F Barker. Towards sympathetic cooling of large molecules: cold collisions between benzene and rare gas atoms. *New Journal of Physics*, 11:055029, 2009.

[29] Martin Zeppenfeld, Barbara G. U. Englert, Rosa Glöckner, Alexander Prehn, Manuel Mielenz, Christian Sommer, Laurens D. van Buuren, Michael Motsch, and Gerhard Rempe. Sisyphus cooling of electrically trapped polyatomic molecules. *Nature*, 491:570–573, November 2012.

[30] D. Gerlich and G. Borodi. Buffer gas cooling of polyatomic ions in rf multi-electrode traps. *Faraday Discuss*, 142:57–72, 2009.

[31] Nicholas R. Hutzler, Hsin-I Lu, and John M. Doyle. The buffer gas beam: An intense, cold, and slow source for atoms and molecules. *Chemical Reviews*, 112:48034827, 2012.

[32] Christoph Jan Schaeff. Elastic slowing of supersonic beams with an atomic mirror. Master's thesis, The University of Texas at Austin, Austin, Texas, US, December 2008.

[33] E. Narevicius, A. Libson, M. F. Riedel, C. G. Parthey, I. Chavez, U. Even, and M. G. Raizen. Coherent slowing of a supersonic beam with an atomic paddle. *Physical Review Letters*, 98:103201, 2007.

[34] Max Fabian Riedel. Elastic slowing of supersonic beams. Master's thesis, The University of Texas at Austin, Austin, Texas, US, December 2006.

[35] Manish Gupta and Dudley Herschbach. Slowing and speeding molecular beams by means of a rapidly rotating source. *J. Phys. Chem. A*, 105:1626–1637, 2001.

[36] Manish Gupta and Dudley Herschbach. A mechanical means to produce intense beams of slow molecules. *J. Phys. Chem. A*, 103:10670–10673, 1999.

[37] Manish Gupta. *A Mechanical Means to Produce Cold, Slow Beams of Molecules*. PhD thesis, Harvard University, Cambridge, Massachusetts, US, May 2000.

[38] M. Strebel, F. Stienkemeier, and M. Mudrich. Improved setup for producing slow beams of cold molecules using a rotating nozzle. *Physical Review A*, 81:033409, 2010.

[39] Susumu Kuma and Takamasa Momose. Deceleration of molecules by dipole force potential: a numerical simulation. *New Journal of Physics*, 11:055023, 2009.

[40] D. DeMille, D.R. Glenn, and J. Petricka. Microwave traps for cold polar molecules. *The European Physical Journal D*, 31:375–384, 2004.

[41] Katsunari Enomoto and Takamasa Momose. Microwave stark decelerator for polar molecules. *Physical Review A*, 72:061403(R), 2005.

[42] Katsunari Enomoto, Pavle Djuricanin, Ilja Gerhardt, Omid Nourbakhsh, Yoshiki Moriwaki, Walter Hardy, and Takamasa Momose. Superconducting microwave cavity towards controlling the motion of polar molecules. *Appl. Phys. B*, 109:149–157, 2012.

[43] Robert M. Hill and Thomas F. Gallagher. Deflection of csf molecules by resonant inhomogeneous electric fields. *Physical Review A*, 12:451–459, 1975.

[44] Simon Merz, Nicolas Vanhaecke, Wolfgang Jäger, Melanie Schnell, and Gerard Meijer. Decelerating molecules with microwave fields. *Physical Review A*, 85:063411, 2012.

[45] Hitoshi Odashima, Simon Merz, Katsunari Enomoto, Melanie Schnell, and Gerard Meijer. Microwave lens for polar molecules. *Physical Review Letters*, 104:253001, 2010.

[46] Zhenxing Gu, Chaoxiu Guo, Shunyong Hou, Shengqiang Li, Lianzhong Deng, and Jianping Yin. Controllable electrostatic surface guide for cold molecules with a single charged wire. *Physical Review A*, 87:053401, 2013.

[47] M. Strebel, S. Spieler, F. Stienkemeier, and M. Mudrich. Guiding slow polar molecules with a charged wire. *Physical Review A*, 84:053430, 2011.

[48] Jacqueline van Veldhoven, Hendrick L. Bethlem, and Gerard Meijer. ac electric trap for ground-state molecules. *Physical Review Letters*, 94:083001, 2005.

[49] Marina Quintero-Pérez, Paul Jansen, Thomas E. Wall, Joost E. van den Berg, Steven Hoekstra, and Hendrick L. Bethlem. Static trapping of polar molecules in a traveling wave decelerator. *Physical Review Letters*, 110:133003, 2013.

[50] E Tsikata, W C Campbell, M T Hummon, H-I Lu, and J M Doyle. Magnetic trapping of nh molecules with 20 s lifetimes. *New Journal of Physics*, 12:065028, 2010.

[51] Matthew T. Hummon, Mark Yeo, Benjamin K. Stuhl, Alejandra L. Collopy, Yong Xia, and Jun Ye. Magneto-optical trapping of diatomic molecules. *arXiv:1209.4069v1*, September 2012.

[52] Marius Lysebo and Leif Veseth. Diatomic molecules in optical and microwave dipole traps. *Physical Review A*, 83:033407, 2011.

[53] Paul M. Baker and James A. Stickney. Adjustable microchip ring trap for cold atoms and molecules. *Physical Review A*, 80:063615, 2009.

[54] Deanne L. Snavely, Steven D. Colson, and Kenneth B. Wiberg. Rotational cooling in a supersonic expansion of ammonia. *The Journal of Chemical Physics*, 74:6975, 1981.

[55] D.R. Miller. *Atomic and Molecular Beam Methods*, volume vol. 1. Oxford University Press, Oxford, 1988.